



An Overview of Nanostructural Tungsten Oxides and Their Nanocomposites for Photoelectrochemical Water Splitting

Journal:	<i>Nanoscale</i>
Manuscript ID	NR-REV-04-2019-003474.R1
Article Type:	Review Article
Date Submitted by the Author:	20-Jun-2019
Complete List of Authors:	<p>Zheng, Guangwei; Beijing University of Technology Wang, Jinshu; Beijing University of Technology, Liu, Hu; Zhengzhou University, NERC Murugadoss, Vignesh; Pondicherry University, Centre for Nanoscience and Technology Zu, Guannan; Beijing University of Technology, College of Materials Science and Engineering Che, Haibing; Beijing University of Technology Chen, Lai; Beijing University of Technology, Materials Science and Engineering Li, Hongyi; beijing university of technology, Ding, Tao; Henan University, College of Chemistry and Chemical Engineering Gao, Qiang; Oak Ridge National Laboratory, Guo, Zhanhu; University of Tennessee Knoxville, Chemical & Biomolecular Engineering</p>

Tungsten Oxide Nanostructures and Nanocomposites for Photoelectrochemical Water Splitting

Guangwei Zheng,^{a,b} Jinshu Wang,^{a,*} Hu Liu^{c,*} Vignesh Murugadoss,^{b,d} Guannan Zu,^a Haibing Che,^a Chen Lai,^a Hongyi Li,^a Tao Ding,^{e,*} Qiang Gao,^{f,*} and Zhanhu Guo^{b,*}

^a *Key Lab of Advanced Functional Materials, Ministry of Education, College of Materials Science and Engineering, Beijing University of Technology, Beijing 100124, China. Email: wangjsh@bjut.edu.cn*

^b *Integrated Composites Laboratory (ICL), Department of Chemical & Biomolecular Engineering, University of Tennessee, Knoxville, TN 37996, United States. E-mail: zguo10@utk.edu*

^c *Key Laboratory of Materials Processing and Mold (Zhengzhou University), Ministry of Education, National Engineering Research Center for Advanced Polymer Processing Technology, Zhengzhou University, Zhengzhou, 450002, Henan, China. E-mail: liuhu@zzu.edu.cn*

^d *Pondicherry University, Centre for Nanoscience and Technology, Puducherry, IN 605014*

^e *College of Chemistry and Chemical Engineering, Henan University, Kaifeng, 475004, Henan China E-mail: dingtao@henu.edu.cn*

^f *Scanning Probe Microscopy Group, Center for Nanophase Materials Sciences, Oak Ridge National Laboratory, P.O. Box 2008, Oak Ridge, TN 37831, United States. Email: gaoq@ornl.gov*

ABSTRACT: Hydrogen production from photoelectrochemical (PEC) water splitting using semiconductor photocatalysts has attracted great attentions to realize clean and renewable energy from solar energy. A visible-light-response WO_3 with a long hole diffusion length (~ 150 nm) and good electron mobility ($\sim 12 \text{ cm}^2 \text{ V}^{-1} \text{ s}^{-1}$) makes it suitable as the photoanode. However, WO_3 suffers from issues including rapid recombination of photoexcited electron-hole pairs, photo-corrosion during the photocatalytic process due to the formation of peroxy-species, sluggish kinetics of photogenerated holes, and slow charge transfer at the semiconductor/electrolyte interface. This work highlights the approaches to overcome these drawbacks of WO_3 photoanodes, including: i) the manipulation of nanostructured WO_3 photoanodes to decrease the nanoparticle size to promote holes migration to WO_3 /electrolyte interface which benefits the charge separation; ii) doping or introducing oxygen vacancies to improve electrical conductivity; exposing high energy crystal surfaces to promote the consumption of photogenerated holes on the high-active crystal face, thereby suppressing the recombination of photogenerated electrons and holes; iii) decorating with co-catalysts to reduce the overpotential which inhibits the formation of peroxy-species; iv) other methods such as coupling with narrow band semiconductors to accelerate the charge separation and controlling crystal phase via annealing to reduce defects. These approaches are reviewed with detailed examples.

1. Introduction

The scarcity and growing demands of fossil fuels requires our society to develop an efficient, clean and renewable energy.¹⁻⁴ Photocatalytic water splitting to produce H₂ has become an effective approach to address those issues.^{5,6} Since pioneering works by Becquerel in 1839⁷ and Fujishima and Honda in 1972,⁸ the photocatalytic and photoelectrochemical (PEC) water splitting using semiconductors under solar irradiation have attracted remarkable attention. Afterwards, various photocatalysts including hematite,⁹ BiVO₄,¹⁰⁻¹² WO₃,¹³⁻¹⁵ TiO₂,^{16,17} ZnO,¹⁸ CdS,¹⁹ TaON,²⁰ IrO₂,²¹ SrTiO₃,^{22, 23} Ta₃N₅,²⁴ and BiFeO₃²⁵ have been exploited as photoanodes. Metal chalcogenides, *e.g.* CdS and MoS₂, have been reported as promising photocatalysts for water splitting because of their narrow band gap,²⁶ while they are more susceptible to degradation during water oxidation reaction. Oxides are the most photochemically stable semiconductors in aqueous solution,²⁷ though TiO₂ and ZnO have a wide band gap energy that can be excited only by UV photons. Among the myriad of oxides, WO₃ with a band gap of 2.4-2.8 eV²⁸ has been considered to be the most promising visible light responsive photoanodes for PEC water splitting. The large valence band (VB) of WO₃ located at approximately 3.0 V *vs.* NHE makes it appropriate for water oxidation. WO₃ possesses a moderate hole diffusion length (~150 nm) compared with α -Fe₂O₃ (2–4 nm) and better electron mobility (~12 cm² V⁻¹ s⁻¹) than TiO₂ (~0.3 cm² V⁻¹ s⁻¹).²⁹ Moreover, the low-cost WO₃ exhibits excellent stability and the carriers move fast under solar irradiation.^{30,31} Nevertheless, the activity of WO₃ for PEC water splitting still needs be improved. As an indirect semiconductor, WO₃ requires a relatively thick film for adequate light absorption which causes a significant recombination of electrons and holes, thus decreases the performance of PEC water splitting.³² During water splitting, the possibly formed peroxy-species on the WO₃ surface accelerate the photo-corrosion and consequently reduce the stability of WO₃ photoanode.^{32,33} The

sluggish kinetics of photogenerated holes and charge transfer at the semiconductor/electrolyte interface intensifies the drawback of WO_3 photoanode.^{29, 34, 35} The maximum theoretical solar-to-hydrogen efficiency of WO_3 is ~6% and the theoretical photocurrent density is 4 mA cm^{-2} under Air Mass 1.5 Global (AM 1.5 G) solar illumination. The WO_3 -based PEC devices cannot compete directly with coupled solar and electrolysis with an efficiency of about 10%. Nevertheless, modified WO_3 -based PEC can potentially achieve efficiencies beyond 10% at a low cost.³⁶ Considerable attempts have been made to solve the issues including doping, orderly nanostructured morphologies, coupling with narrow band semiconductors, introducing oxygen vacancies, and decorating with co-catalysts, etc.

Previous reviews have been presented regarding the use of WO_3 in electrochromic, photochromic, gas sensors and photocatalytic degradation. However, the strategies to improve the performance of WO_3 photoanodes for PEC water splitting have been rarely summarized. In this review, recent progresses in the WO_3 photoanodes and the possibility of using WO_3 for the direct Z-scheme overall water splitting were documented with detailed examples. The strategies to overcome the limitations of WO_3 as photoanodes were summarized to enhance the photocatalytic activity for PEC water splitting with detailed examples. (1) The PEC water splitting performance of WO_3 suffers from the recombination of electron-hole pairs. WO_3 nanostructures with small sizes and controllable morphologies can decrease the diffusion length of holes and reduce the grain boundaries to benefit the charge separation.³⁷ Doping with a hetero-element or introducing oxygen vacancies can improve electrical conductivity and facilitate charge transfer.³⁸ Moreover, exposing high energy crystal surfaces can promote the consumption of photoexcited holes on the high-active crystal face, which reduces the recombination of photogenerated electron-hole pairs.³² Coupling with narrow band gap semiconductor can form an internal electric field at the interface which

facilitates the separation of photogenerated electrons and holes and restricts the recombination.³⁹ (2) During oxygen evolution reaction (OER), peroxy species formed and accumulated on the surface of WO_3 become kinetically competitive with O_2 production, thus result in the photo-corrosion. Decorating with co-catalysts can improve the surface kinetics and reduce the OER overpotential that inhibits the formation of peroxy species.⁴⁰ The optimized crystallinity and exposing highly active crystal surface can impede the formation of peroxy species on the surface of WO_3 .⁴¹ (3) Although coupling with a narrower band gap semiconductor to form II heterojunctions can improve the PEC water splitting performance, it is limited to realize overall water splitting without changing the original oxidation and reduction potential. To achieve overall water splitting efficiency, coupling with a narrow bandgap semiconductor to create direct Z-scheme system can significantly promote an efficient charge separation as well as maintain the optimized redox ability.

2. Photocatalytic and PEC water splitting mechanism

The fundamental principle of one-step overall water splitting on semiconductor is shown in Fig. 1a. Under light irradiation with an energy no less than the band gap of a semiconductor, electrons excited from the VB move to the conduction band (CB), leaving holes in the VB.⁴² Under standard conditions, the overall water splitting is an uphill reaction requiring a Gibbs free energy of $\Delta G = +237.2 \text{ kJ mol}^{-1}$ corresponding to the electrolysis cell voltage of $\Delta E^0 = 1.23 \text{ V}$ per electron transferred according to the Nernst equation.⁴³ To split the water into H_2 and O_2 , the band-gap energy of the semiconductors should be larger than 1.23 eV. In other words, the CB of the semiconductor should be more negative than 0 V vs. NHE, while the VB of the semiconductor has to be more positive than 1.23 V vs. NHE.^{44, 45} The band gap of the semiconductor should be narrower than 3 eV to achieve visible-light-response sufficiently.⁴⁶ The semiconductor must be

stable in the photocatalytic reaction. At least, the photogenerated carriers transferred from the surface of semiconductor to the solution must be facile enough to reduce energy loss arising from the kinetic overpotential.⁴⁷ In this regard, only very few semiconductors are suitable for one-step water splitting.

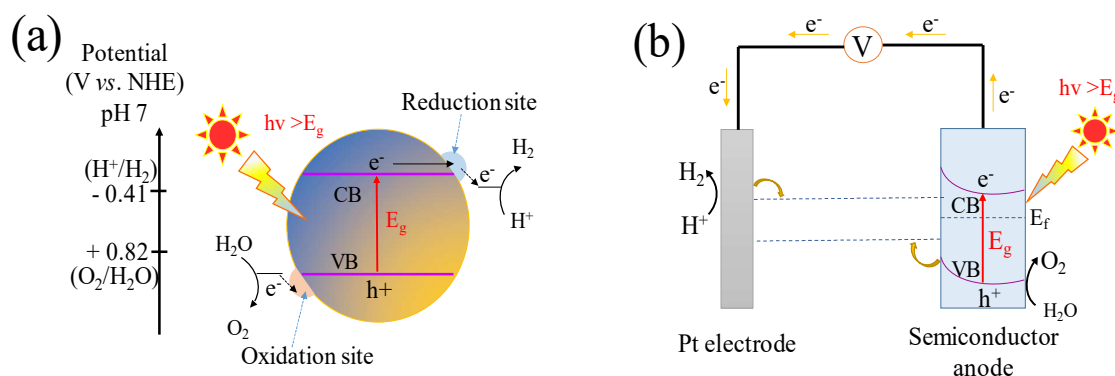
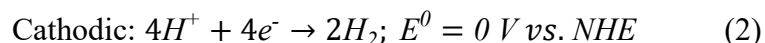


Fig. 1 Schematic illustration of (a) photocatalytic water splitting for a one-step photoexcitation system, (b) The basic principles of water splitting for a PEC cell with an n-type semiconductor photoanode and Pt cathode. CB, conduction band; VB, valence band; E_g , band gap; E_f , fermi level.

PEC is the other approach to achieve overall water splitting in which semiconductor is employed as photoanode and Pt always as the counter electrode, both are immersed in an aqueous electrolyte. In this system (Fig. 1b), a bias potential is applied to facilitate the separation of the photoexcited electron-hole pairs due to the formation of depletion layer in the photoanode. Meanwhile, the applied bias shifts the electrode potential of the metal cathode sufficiently negative of the reversible hydrogen potential and thereby enables the proton reduction.⁴⁸ It is thus likely for the narrow band gap semiconductor with a CB lower than the energy of H^+/H_2 to produce hydrogen. Hence many semiconductors were used as photoanodes for the PEC overall water splitting including WO_3 , despite more positive location of its CB (0.55-0.8 V vs. RHE (reversible hydrogen electrode), pH=0).⁴⁹ In the PEC water-splitting cells, hydrogen is produced at the

cathode and oxygen evolution at the anode, thus the well physically separated chambers of hydrogen and oxygen can be achieved. This process of PEC water splitting can be summarized by Equations (1&2):⁵⁰



The PEC water splitting reaction normally occurs in three steps: i) the photoanode semiconductor absorbs the photon energy that is higher than the band gap of the semiconductor to excite the electron-hole pairs in the bulk; ii) the separation of photogenerated charges, *i.e.*, the holes reach the surface of photoanode to oxidize water molecules into O₂ whereas the electrons migrate to the counter electrode to reduce water molecules into H₂; iii) the recombination of photogenerated holes and electrons, inducing a back-electron flow from the external circuit into the photoelectrode.⁵¹ The first two steps strongly depend on the structure and electronic properties of the photocatalyst. Concerning the third step, the recombination of holes and electrons restricts the photoconversion efficiency. Therefore, it is significantly necessary to develop a promising visible light response and create highly efficient photocatalysts for the overall water splitting.

In the PEC water splitting system, the photocurrent density as a function of potential is an important parameter to evaluate its performance. The theoretical photocurrent density of WO₃ is reported to be 4 mA cm⁻² under AM 1.5 G.³² In a three-electrode system using Ag/AgCl as a reference electrode, the measured electrode potentials *vs.* Ag/AgCl could be converted to the RHE potential according to the Nernst equation:^{32, 52}

$$E_{RHE} = E_{Ag/AgCl} + 0.059 \times pH + E_{Ag/AgCl}^0 \quad (3)$$

where E_{RHE} refers to the calculated potential vs. RHE, $E_{\text{Ag/AgCl}}$ is the measured potential vs. Ag/AgCl, and the value of $E_{\text{Ag/AgCl}}^0$ is 0.197 V at 25 °C.

Another important factor for evaluating photoactive behavior is the incident photon-to-current efficiency (IPCE), representing the photocurrent collected per incident photon flux as a function of incident-light wavelength. The IPCE could be calculated at a desired bias voltage from eqn (4):^{52, 53}

$$IPCE = \frac{1240J}{\lambda \times I} \times 100\% \quad (4)$$

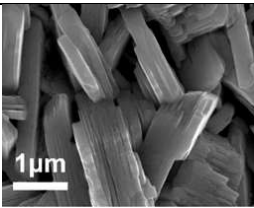
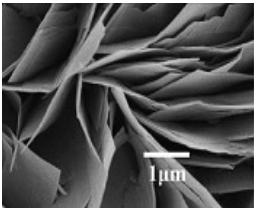
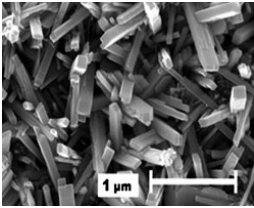
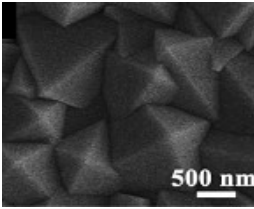
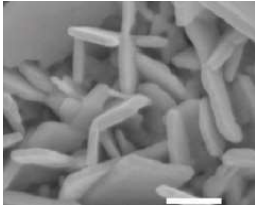
where J is the photocurrent density (mA cm^{-2}) under illumination at wavelength λ , λ is the wavelength of incident light (nm), and I corresponds to the incident light intensity (mW cm^{-2}).

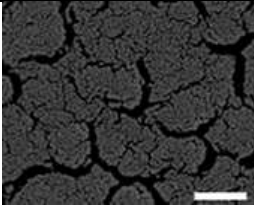
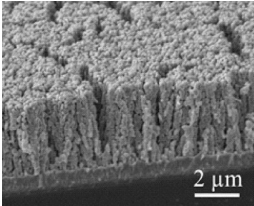
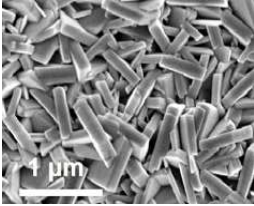
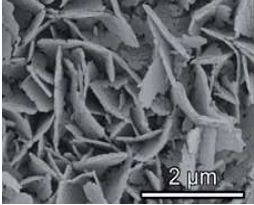
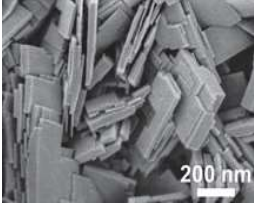
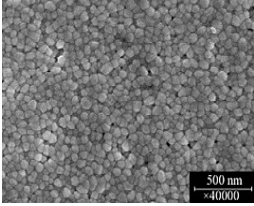
3. Strategies to enhance WO_3 photocatalytic activity in PEC water system

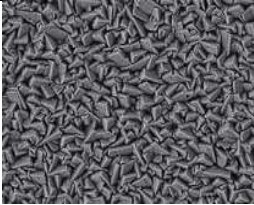
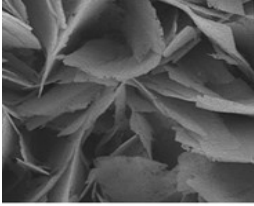
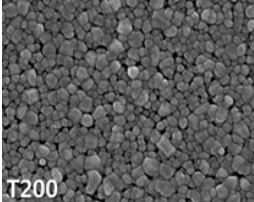
3.1. Morphological manipulation. Compared with bulk materials, nanostructured materials with higher specific surface area and more reaction active sites can enhance the photon absorption to improve the photoelectric conversion efficiency.^{37, 54} The size of bulk WO_3 is larger than 150 nm, and restricts the holes migration to the surface of WO_3 . Thanks to a shorter hole transport distance, the nanomaterials could improve the separation efficiency of photogenerated electron-hole pairs and give a more rapid photoexcited hole injection to the electrolyte. However, small grains can reduce the activity in the visible light region.⁵⁵ Furthermore, the defects on the crystal surface make it possible for intensive electron-hole recombination which reduces the PEC water splitting performance.³⁴ Thus, developing appropriate grain size, structure and morphology of the photocatalyst holds the key to improve the photocatalytic performance. The widely used methods for synthesizing WO_3 nanostructures include solvothermal,⁵⁶ hydrothermal,^{57, 39}

anodization,⁵⁸ glancing angle deposition (GLAD),⁵⁹ pulsed laser deposition (PLD),⁶⁰ sol-gel,⁶¹ chemical vapor deposition (CVD),⁶² and electrodeposition.⁴⁰ Meanwhile, the fabrication methods were found to affect the grain boundaries and the dimension of the nanostructures, which limited the efficiency of water splitting. The morphology, fabrication method and PEC water splitting performance of the WO₃ photoanode films have been illustrated in Table 1. Amongst the myriad, hydrothermal/solvothermal techniques have been commonly used to synthesize nanostructure WO₃ film. During the synthesis, introducing a very thin WO₃ dense layer has been found to be a prerequisite for the crystal growth that can hinder the interfacial recombination and decrease the photogenerated electron injection back into the electrolyte on the exposed areas of FTO.^{59, 63} Meanwhile, involving seed layers contributes to form grain boundaries in the nanocrystalline base film which can reduce the photocatalytic activity.⁶⁴⁻⁶⁶

Table 1. Representative morphology of WO₃ photoanode for PEC water splitting.

Topography	Fabrication method	Film texture	Photoelectrochemistry	Ref
Nanoplate	2-step hydrothermal		Photocurrent: 3.7 mA cm ⁻² at 1.23 V vs. RHE; IPCE: 67% at 350 nm at 1.23 V vs. RHE; electrolyte: 0.1 M Na ₂ SO ₄	32
Nanoflake	Solvothermal		Photocurrent: ~1.43 mA cm ⁻² at 1.23 V vs. RHE; IPCE: ~70% at 480 nm at 1.23 V vs. RHE; electrolyte: 0.1 M Na ₂ SO ₄	56
Nanorod	Hydrothermal		Photocurrent: 2.26 mA cm ⁻² at 1.23 V vs. RHE; IPCE: ~90% at 350 nm at 1.23 V vs. RHE; electrolyte: 0.5 M H ₂ SO ₄	57
Microcrystal	Hydrothermal		Photocurrent: 0.45 mA cm ⁻² at 0.8 V vs. RHE; IPCE: ~2.7% at 300 nm at 0.8 V vs. RHE; electrolyte: 1 M H ₂ SO ₄	39
Nanoflake	Anodization		Photocurrent: 0.9 mA cm ⁻² at 1.2 V vs. RHE; IPCE: ~42% at 420 nm at 1.2 V vs. RHE ; electrolyte: 0.5 M H ₂ SO ₄	58

Nanorod	Glancing angle deposition (GAD)		Photocurrent: 2.15 mA cm ⁻² at 1.23 V vs. RHE; IPCE: ~40% at 385 nm at 1.23 V vs. RHE; electrolyte: 0.5 M KPi + 1 M Na ₂ SO ₃	59
Tree-like nanoporous	Pulsed laser deposition (PLD)		Photocurrent: 1.8 mA cm ⁻² at 1.23 V vs. RHE; IPCE: ~78% at 350 nm at 1.23 V vs. RHE ; electrolyte: 0.5 M KPi + 0.5 M H ₂ SO ₄	60
Nanoplate	Water bath		Photocurrent: ~1.42 mA cm ⁻² at 1.23 V vs. RHE; IPCE: ~38% at 400 nm at 1.23 V vs. RHE; electrolyte: 0.1 M Na ₂ SO ₄	41
Nanoflake	Hydrothermal		Photocurrent: 2.25 mA cm ⁻² at 1.23 V vs. RHE; IPCE: ~23.25% at 440 nm at 1.23 V vs. RHE electrolyte: 0.1 M Na ₂ SO ₄	67
Nanoplate	Hydrothermal		Photocurrent: 1.2 mA cm ⁻² at 1.23 V vs. RHE; IPCE: ~40% at 350 nm at 1.23 V vs. RHE electrolyte: 1 M H ₂ SO ₄	68
Nanoparticle	Hydrothermal		Photocurrent: 2.7 mA cm ⁻² at 1.4 V vs. RHE; electrolyte: 0.5 M H ₂ SO ₄	69

Nanoneedle	Pulsed laser deposition (PLD)		Photocurrent: 2.4 mA cm ⁻² at 1.23 V vs. RHE; IPCE: 50% at 410 nm at 1.23 V vs. RHE; electrolyte: 0.1 M H ₂ SO ₄	70
Nanoflake	Solvothermal		Photocurrent: 1.1 mA cm ⁻² at 1.23 V vs. RHE; IPCE: ~45% at 320 nm at 1.23 V vs. RHE; electrolyte: 0.1 M Na ₂ SO ₄	71
Nanoparticle	Polymer-assisted deposition		Photocurrent: 1.45 mA cm ⁻² at 1.23 V vs. RHE; electrolyte: 0.1 M KPi	72

Note: WO₃ is only stable in acidic media of pH lower than 4. That is, the PEC properties of WO₃ may be investigated unstable in the electrolyte with 4 < pH ≤ 7. Researchers should investigate the PEC performance of WO₃ under strong acidic conditions in the future work.

3.1.1. 1-D WO₃ nanostructures. Due to the direct pathways for photogenerated carriers, one dimensional (1-D) semiconductor structures, *e.g.*, nanowires,^{56, 62, 73-75} nanorods,^{57, 76-78} nanotubes,⁷⁹ and nanoneedles⁸⁰, can efficiently facilitate the transportation of photoelectrons to FTO and thus suppress the recombination of photogenerated electron-hole pairs. These structures are capable of reducing grain boundaries and defects that result in less recombination of electron-hole pairs,⁵⁶ and consequently 1-D WO₃ nanostructure photoanodes demonstrated superior PEC properties compared to nanocrystalline particles.⁸¹⁻⁸⁴ For example, Chakrapani *et al.*⁶² fabricated WO₃ nanowire (length: 2-3 μm and diameter: 40-70 nm) arrays on FTO substrate via chemical vapor deposition in ambient air. The blue film changed to greenish yellow corresponding to the crystal phase change from monoclinic to orthorhombic phase. Under light irradiation AM 1.5 G,

the WO₃ nanowire arrays exhibited a photocurrent of 1.2 mA cm⁻² at 1.2 V vs. SCE. These nanowires could capture the incident light more efficiently to enhance the PEC performance. Joo *et al.*⁵⁷ synthesized single crystalline structure WO₃ nanorods uniformly distributed on the FTO substrate using a facile hydrothermal method without the assistance of any seed layer. After annealed at 500 °C, these nanorods exhibited an outstanding photocurrent of 2.26 mA cm⁻² at 1.23V vs. RHE and IPCE value of 35% under light irradiation at 400 nm. The excellent PEC performance was attributed to the direct pathway provided by the vertically aligned nanorod arrays on FTO with a desirable crystal phase.

3.1.2. 2-D WO₃ nanostructures. A large number of grain boundaries in the nanoparticle films increase the resistance and interfacial charge recombination, and thus impede the electron transfer to the back-contacted conductive substrate.⁶⁴ Different from nanoparticles and similar to 1D semiconductor structures, 2D nanostructures, *e.g.*, nanoplates,^{64, 65, 85-87} nanosheets,^{88, 89} and nanoflakes, are favorable for highly efficient and directional transport of electrons and holes.^{64, 85, 90} Besides, 2D semiconductors have a bigger surface/volume ratio than 1D semiconductor.⁹¹ WO₃ nanoplates are reported to exhibit an enhanced PEC performance compared with nanorods and nanowires.^{56, 92} Su *et al.*⁵⁶ synthesized WO₃ nanowire and nanoflake under almost the same conditions via a seed-layer-assistant solvothermal method. Both nanowire and nanoflake were well vertically grown on the substrate (Fig. 2a-c). The WO₃ nanoflake photoanodes demonstrated a significantly higher PEC performance than WO₃ nanowires. The band gaps of the WO₃ nanowire and WO₃ nanoflake were calculated to be 2.92 and 2.51 eV, respectively. Under the same photocurrent measurement conditions, the WO₃ nanoflake film delivered about 3 times higher photocurrent than that of the nanowire film with a comparable thickness (Fig. 2e). Meanwhile, the WO₃ nanoflake films exhibited a higher IPCE value compared to the WO₃ nanowire film (Fig. 2f).

The excellent photoelectric performance originated from the lower band gap of WO₃ nanoflake and reduced light scattering in the flake array structure (Fig. 2d). Under light irradiation below 400 nm, the WO₃ nanoflakes with a thickness of 5.6 μm were found to exhibit a higher photocurrent value of 1.43 mA cm⁻² and a higher IPCE value of higher than 60%.

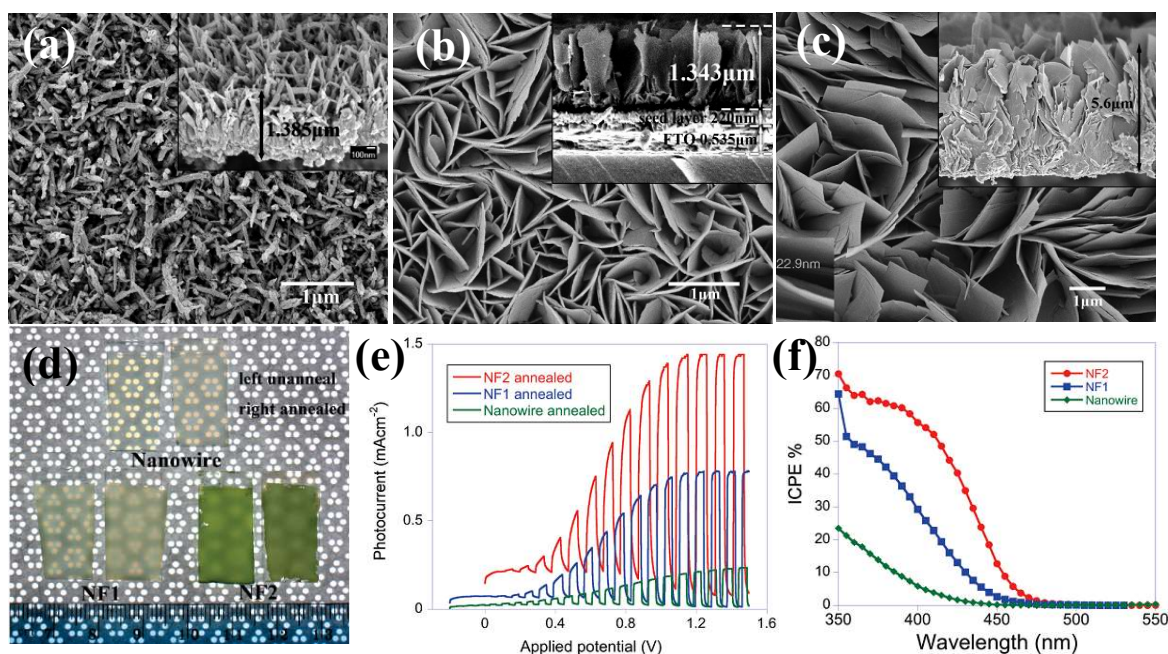


Fig. 2 FESEM images of (a) Unannealed WO₃ nanowire, (b) Unannealed WO₃ nanoflake (NF1) (c) Unannealed WO₃ nanoflake (NF2), (d) Photograph of WO₃ films as-prepared and after anneal, (e) Current-potential plots for annealed nanowire, and two flake samples, under chopped visible light in an aqueous solution of 0.1 mol/L sodium sulfate (Na₂SO₄), (f) IPCE of three samples with a bias of 0.5 V in a two electrode setup with Pt foil as counter electrode. Reproduced from ref. ⁵⁶ Copyright 2011 American Chemical Society

3.1.3. Nanoporous structure. Compared with bulk material, the nanostructured semiconductors with high porosity have shown a better photoelectricity activity due to their large specific surface areas, more active sites, higher light absorption rate and excellent charge transport performance.⁹³⁻⁹⁶ With a larger specific surface area, it could facilitate ion transport into nanostructured photoelectrodes. Furthermore, the nanoporous structure increases the area of depletion layer and

shortens the distance of diffusion for holes to the photoelectrodes/electrolyte interface, thereby inhibiting surface recombination of electrons and holes.^{60, 97, 98} However, there are some adverse effects when increasing the surface area. For example, the increased surface defects and grain boundaries may be formed, thereby reducing the photocatalytic activity. Therefore, it is crucial to design photoanodes with optimal active sites for photo activities.⁵⁹ Shin *et al.*⁶⁰ prepared nanoporous WO₃ having tree-like structure via a pulsed laser deposition method. The photoanodes have a monoclinic WO₃ crystal structure and are partially aligned along the [020] direction. Moreover, the nanoporous WO₃ showed 9-fold photocurrent density compared to the dense WO₃. The improved PEC performance can be mainly attributed to a higher surface/active area of the nanoporous structure, which allowed the electrolyte to permeate through the open channels to reduce the transport distance of holes, and restrained the recombination of surface electron-hole. Song *et al.*⁹⁹ used versatile foaming-assisted electrospinning method to prepare mesoporous WO₃ nanobelts which enhanced the PEC water splitting performance compared with the as-prepared WO₃ nanofiber and WO₃ nanobelt samples. Hilliard *et al.*¹⁰⁰ synthesized mesoporous WO₃ via a facile sol-gel dip coating method. Compared with dense WO₃ thin films, the mesoporous WO₃ photoanode exhibited a more substantial photocurrent response which was ascribed to massive specific surface area exposure to the electrolyte. It confirmed that the surface oxidation kinetics, optical absorption and conductivity of WO₃ limited the PEC activity of the mesoporous WO₃ photoanodes. Concerning neutral or basic solutions, the peroxy species formed on the surface of WO₃ reduced the stability of photoanodes.

3.1.4. Hierarchical 3D structure. Apart from the aforementioned morphologies, new structures and hierarchical 3D WO₃ photoanodes were designed to provide high solar conversion efficiencies. For example, Feng *et al.*²⁹ synthesized sandwich structured WO₃ nanoplate arrays via

hydrothermal method followed by annealing at 500 °C. The sandwich structure exhibited an optimal PEC performance with a photocurrent density of 1.88 mA cm⁻² at 1.3 V vs. Ag/AgCl. The highest PEC performance of the sandwich structured WO₃ compared with other samples annealed at different temperatures arose from more active monoclinic phase, the smallest interface resistance and the largest electrochemically active surface area. Cai *et al.*¹⁰¹ reported another important strategy to prepare hierarchical 3D WO₃ micro-nano architectures which could be easily tuned from porous nanoparticle aggregates (WO₃ PAs) to nanowire aggregates (WO₃ NWs) by controlling the heating temperatures during the thermal oxidation (Figure 3a-d). With increasing the temperatures, the photocurrent density of three types WO₃ nanostructures was decreased (Fig. 3e) due to the decreased exposure of (002) facets. The porous nanoparticle structure annealed at 600 °C significantly enlarged the specific surface area and promoted the electrolyte penetration into electrode and the bottom of aggregates, thereby improved the PEC performances (Fig. 3f).

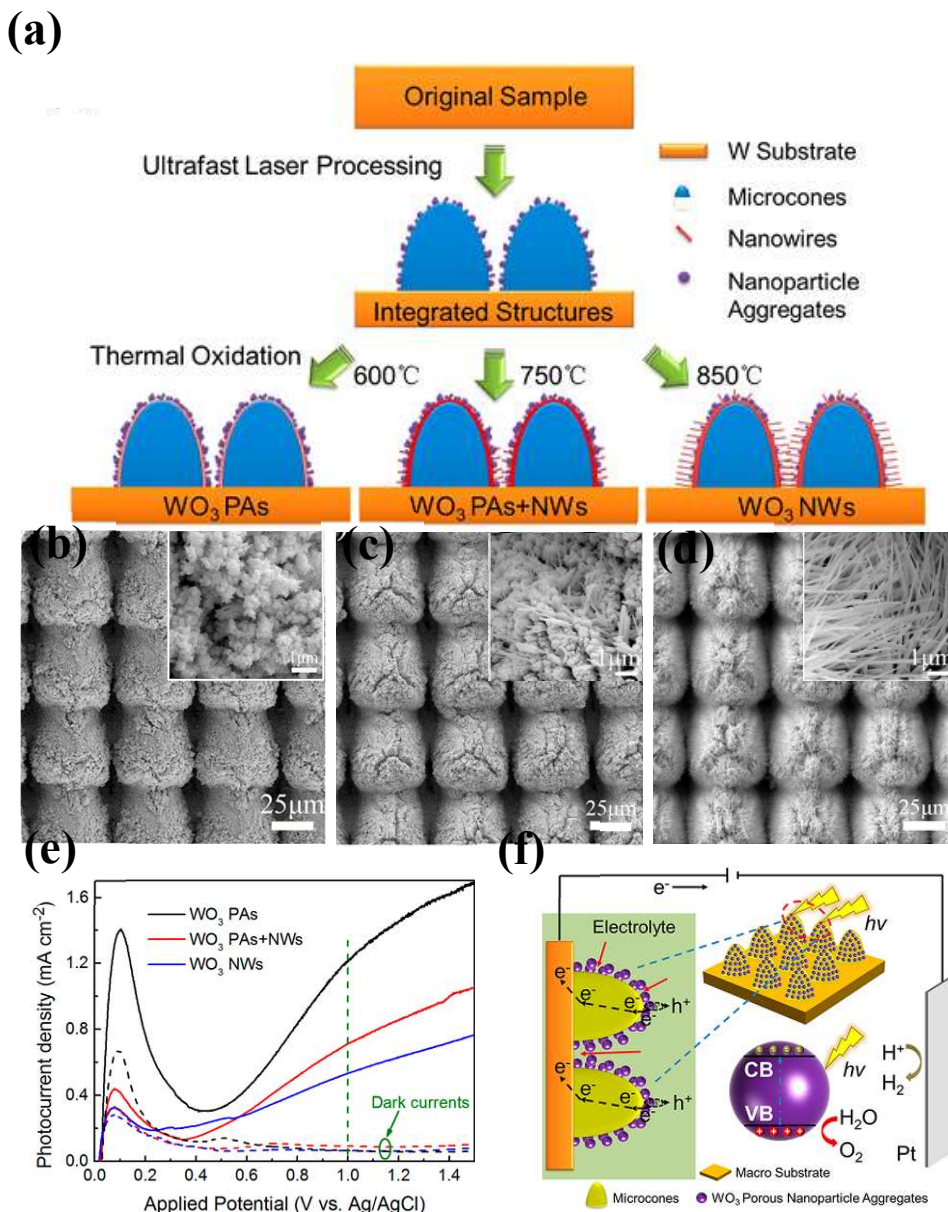


Fig. 3 (a) Schematic of the strategy of tuning WO_3 nanostructures. SEM images of (b) WO_3 PAs, (c) WO_3 PAs+NWs and (d) WO_3 NWs in different magnifications, (e) Photocurrent density of three types of WO_3 nanostructures vs potential plots, (f) Schematic of the hierarchical structure with porous WO_3 nanoparticle aggregates and the corresponding charge transport/transfer and electrolyte permeation processes. The olive color and the arrows represent the electrolyte (0.1 M H_2SO_4) and the penetration of the electrolyte, respectively. Reproduced from ref. ¹⁰¹ Copyright 2017 American Chemical Society

3.2. Crystal phase control. An efficient PEC water splitting performance depends on the photoanode not only the morphology but also the crystal phase of WO_3 . The monoclinic phase of WO_3 has been demonstrated as the most stable phase at room temperature and its water oxidation activity is stronger than that of hexagonal phase or orthorhombic phase WO_3 .^{29, 57, 77, 41, 102-104} With increasing the annealed temperatures, the $\text{WO}_3 \cdot 0.33\text{H}_2\text{O}$ synthesized from precursor changed from orthorhombic to anhydrous hexagonal and then to stable monoclinic (Fig. 4c). As the heating temperature increased from 400 to 500 °C, the absorption edge showed a continuous red shift and the film turned from greyish to yellow (Fig. 4a). The orthorhombic $\text{WO}_3 \cdot 0.33\text{H}_2\text{O}$ demonstrated the lowest photocurrent density, while the monoclinic WO_3 annealed at 500 °C exhibited an optimal PEC performance (Fig. 4b).^{29, 57, 64, 65, 77, 82, 41}

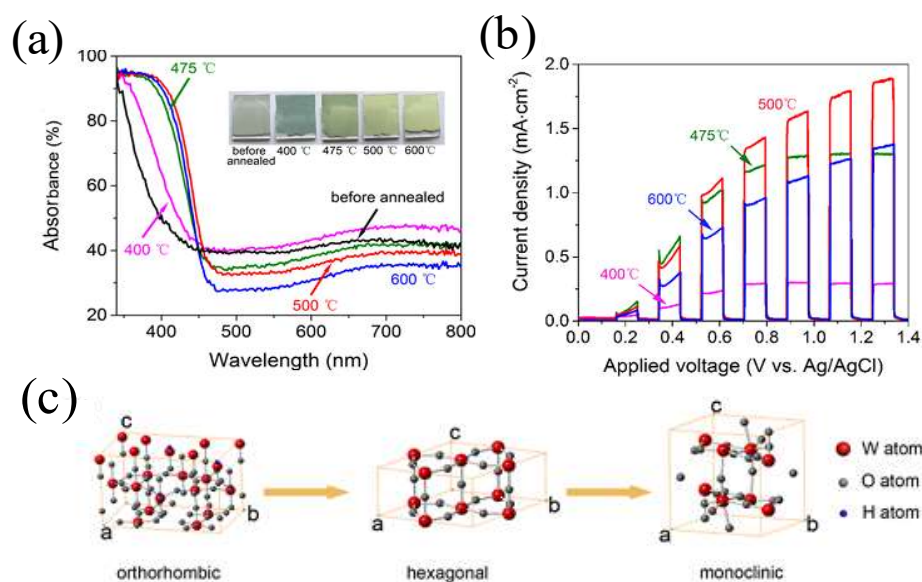


Fig. 4 (a) UV–vis absorption spectra of WO_3 films before and after annealing at different temperatures. The inset is the corresponding photographs, (b) Linear sweep voltammetry of WO_3 photoanodes annealed at different temperatures under chopped incident light, (c) Schematic illustration of unit cells of orthorhombic $\text{WO}_3 \cdot 0.33\text{H}_2\text{O}$, hexagonal WO_3 , and monoclinic WO_3 . Reproduced from ref. ²⁹ Copyright 2016 American Chemical Society.

Nayak *et al.*¹⁰⁵ synthesized $\text{WO}_3 \cdot \text{H}_2\text{O}$ nanoplates via a facile precipitation method, which were evolved into WO_3 nanowires on subsequent solvothermal treatment (Fig. 5a-d). The $\text{WO}_3 \cdot \text{H}_2\text{O}$ nanoplates had an orthorhombic phase, while WO_3 nanowires showed a monoclinic phase (Fig. 5e). The WO_3 nanowires exhibited outstanding PEC activity with a photocurrent density ~ 21 times higher than the $\text{WO}_3 \cdot \text{H}_2\text{O}$ nanoplates. As above discussed, (session 3.1), the nanoplates (2-D nanostructure) normally have a higher photocurrent value than nanowire (1-D nanostructure). The significantly enhanced PEC performance of WO_3 nanowires was attributed to different phases between $\text{WO}_3 \cdot \text{H}_2\text{O}$ nanoplates and WO_3 nanowires. The high crystallinity of WO_3 nanowires reduced the interfacial charge transfer resistance, and thereby improved the PEC performance.

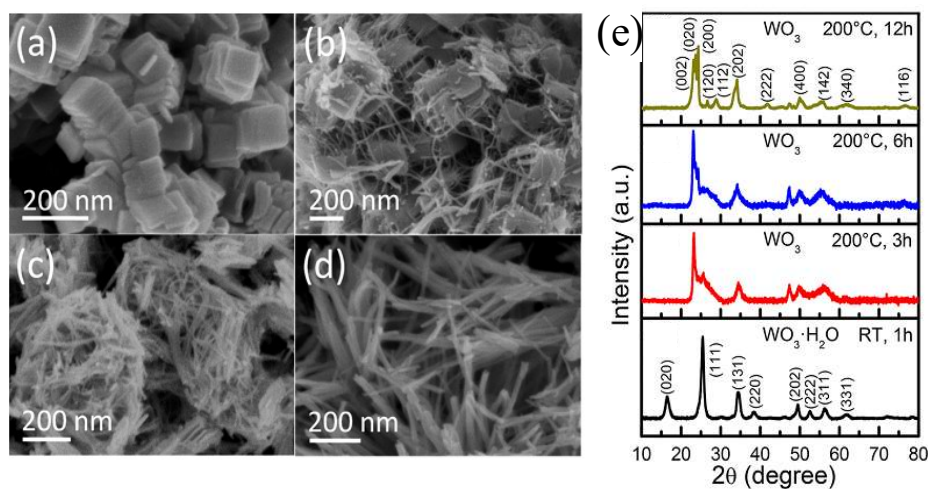


Fig. 5 FESEM images of (a) stacked $\text{WO}_3 \cdot \text{H}_2\text{O}$ square nanoplates synthesized at room temperature using 0.025 M of WCl_6 solution in ethanol for 1 h. FESEM images of WO_3 nanowires evolving from stacked $\text{WO}_3 \cdot \text{H}_2\text{O}$ nanoplates after (b) 3 h, (c) 6 h, and (d) 12 h solvothermal treatment of $\text{WO}_3 \cdot \text{H}_2\text{O}$ nanoplates at 200°C in ethanol. (e) XRD patterns of these obtained samples. Reproduced from ref.¹⁰⁵ Copyright 2017 American Chemical Society

Extensive research efforts have been made to explain the effects of crystal phase on the photocatalytic performance. For example, Park *et al.*⁸² reported that during the annealing process, with the transformation of the crystal phase, the removal of water induced the surface disorder or oxygen deficiencies of WO_3 and thus affected the PEC performance. Zeng's group considered that peroxy species were easily formed on the surface of $\text{WO}_3 \cdot \text{H}_2\text{O}$ due to its inferior crystallinity, while WO_3 annealed at 500 °C had the highest current density because of the conversion of exposed (200) facets to highly reactive (002) facets, superior crystallinity and fewer defects to decrease the recombination of electron-hole pairs.⁴¹ This suggestion was also confirmed by Su's group.¹⁰⁴ Fan's group⁷⁷ suggested that the monoclinic WO_3 obtained at 500 °C (WO_3 -500) exhibited a red shift of the absorption edge which effectively separated the photoexcited electrons and holes and migrated the carriers to the photoanode surface. The existence of both orthorhombic and monoclinic phase along with defects for WO_3 -450 sample and the collapse of nanorods for WO_3 -550 restricted the efficient separation and migration of charge carriers. Yang *et al.* attributed the enhanced PEC properties to the higher crystallinity and the reduced PEC properties for WO_3 calcined at temperatures higher than 500 °C due to the highly damaged surface of the platelets.⁶⁴ The improved crystallinity via high calcination temperature facilitating a better charge separation was also proved by Nuraje's group in the photocatalytic of SrTiO_3 .²³ Thus, it can be concluded that the as-prepared hydrated tungsten oxide needs be calcined at 500 °C to obtain monoclinic WO_3 for an optimal PEC.

3.3. Engineering of crystalline structures. Recent studies on the semiconductor surface engineering have demonstrated that photoexcited electrons and holes can be driven by different crystal planes. Therefore, certain crystal faces of semiconductors will be preferentially reduced, while other crystal faces are preferentially oxidized.¹⁰⁶ Controlling and exposing some high energy

crystal surfaces can improve the photocatalytic and PEC efficiency of photoelectrodes.^{107, 108} Compared with the (200) facet (1.43 J/m²) and the (020) facet (1.54 J/m²), the (002) facet of WO₃ possesses the highest surface energy (1.56 J/m²),¹⁰⁹ which is more favorable for adsorbing the reaction species on the (002) facet to decrease the surface energy. It is verified by Wang *et al.* through density functional theory (DFT) calculations.³² Due to the weakest W-O bond in the monoclinic WO₃, the dangling O atoms on the (002) crystal plane could provide more abundant active sites for H₂O and organics through the hydrogen bond. Therefore, photo-excited holes are more easily consumed on the (002) crystal plane involving the oxidization of water and the degradation of organics by generating active oxygen species, thereby impede the recombination of photogenerated electrons and holes. Consequently, exposure of highly reactive facets could effectively improve the PEC performance in water splitting and the degradation activity of organic pollution.^{92, 110, 111}

Zeng's group⁴¹ prepared WO₃ nanoplate array film photoanodes with a preferential orientation of highly reactive (002) facets by the reduction of peroxotungstates. The effects of synthesis time, temperature, and the amount of the capping agent on the morphologies and nanostructures of the as-prepared WO₃ films were discussed. The TEM images and SAED patterns indicated that the WO₃·H₂O plates grew along the crystal of (020) face which were converted into WO₃ plates with preferentially exposed (002) facets via annealing. The sample annealed at 500 °C exhibited the highest photocurrent density which was ~1.42 mA cm⁻² at 1.23 V *vs.* RHE. The enhanced performance of PEC water splitting was ascribable to the superior crystallinity which could impede the formation of peroxo species on the surface of WO₃. The exposed highly reactive (002) facets of WO₃ nanoplate significantly improved the performance of PEC water splitting. WO₃ photoanodes decorated with Co-Pi co-catalyst improved the water oxidation kinetics and

reduced the photocorrosion resistance. Zhang *et al.*⁹² synthesized monoclinic WO₃ nanomultilayers with (002) facets exposed via a solvothermal method. The sandwiched WO₃ nanomultilayers exhibited photocurrent densities higher than the WO₃ nanorods synthesized as reference. The specific surface area of WO₃ nanorods and nanomultilayers indicated that morphology is not the decisive factor for the enhanced photocurrent of the nanomultilayers. It is the preferentially exposed highly reactive (002) facets of WO₃ nanomultilayers that contributed to the improved PEC water splitting performance.

Although WO₃ exhibits high stability and resistance against photo-corrosion in acid under solar illumination,^{52, 92} WO₃ nanostructures still suffer from photocorrosion and photocatalytic deactivation because of the formation and accumulation of peroxy species on the surface of WO₃.^{112, 33, 59} In a PEC water splitting, photogenerated holes can cause a series of oxidation reactions, including the oxidation of surface hydroxyl groups of WO₃ or the oxidation of water/hydroxide. During the water oxidation reaction, oxygen and peroxy species will be formed. Thermodynamically, the photo-oxidation of water to oxygen ($E^0 = 1.23$ V) is more feasible than the formation of peroxy species ($E^0 = 1.78$ V). However, the peroxy species become kinetically competitive with oxygen evolution because of slow kinetics of oxygen evolution reaction. More importantly, the formation of peroxy species at the WO₃ surface can cause an obvious alternate photo-oxidation reaction, which may result in the loss of photoactivity or photodissolution of WO₃. To address the aforementioned issues, Wang *et al.*³² synthesized WO₃ nanoplates with highly reactive (002) oriented facets via a 2-step hydrothermal method and evaluated the PEC conversion performance (Fig. 6a-f). The 1-step-16h WO₃ nanoplates were prepared via hydrothermal method for 16 h. While, the 2-step-16h WO₃ nanoplates were obtained through the 1-step-8h WO₃ nanoplates after hydrothermal treatment for another 8 h. All of the nanoplates were composed

of dense and vertically aligned nanoplate arrays (Fig. 6a-c). The XRD spectra shown that the 1-step-16h WO_3 nanoplates were mainly exposed (200) facets (Fig. 6d) and the 2-step-16h WO_3 nanoplates were enriched (002) facets (Fig. 6f). During the 1-step-16h hydrothermal reaction, the WO_3 nanoplates mainly had the exposed (002) facets at the initial 8 h of hydrothermal reaction and were then converted into (200) facets exposed in the subsequent 8 h of hydrothermal reaction. This transformation can be explained by the theory of dissolution and recrystallization. Different from the 1-step-16h WO_3 nanoplates, only a partial recrystallization occurred for the 2-step-16h WO_3 nanoplates, which resulted in a larger (200)/(002) ratio. The prepared 2-step-16h WO_3 nanoplates exhibited a remarkable photocurrent density of 3.7 mA cm^{-1} (1.23 V vs. RHE) which corresponded to $\sim 93\%$ of the theoretical photocurrent of WO_3 (Fig. 6g). The curves of chopped transient photocurrent density vs. time showed that the WO_3 nanoplates prepared by 2-step hydrothermal method exhibited the highest photocurrent density and the best stability (Fig. 6h). DFT calculations together with experimental studies demonstrated that the exposing highly reactive (002) facet and nanoplate structures facilitated the separation of photoelectron-hole pairs and suppressed the formation of peroxy-species on the surface, thus enhanced the PEC activity and retained a better photo-stability (Fig. 6i). As a result, the highly oriented (002) crystal plane could significantly improve the PEC water splitting performance and the stability. Accompanied with the 2-D nanostructure and high active crystal monoclinic phase, more research should be focused on the use of 2-D monoclinic WO_3 with a preferentially exposed (002) crystal plane for PEC water splitting in the future.

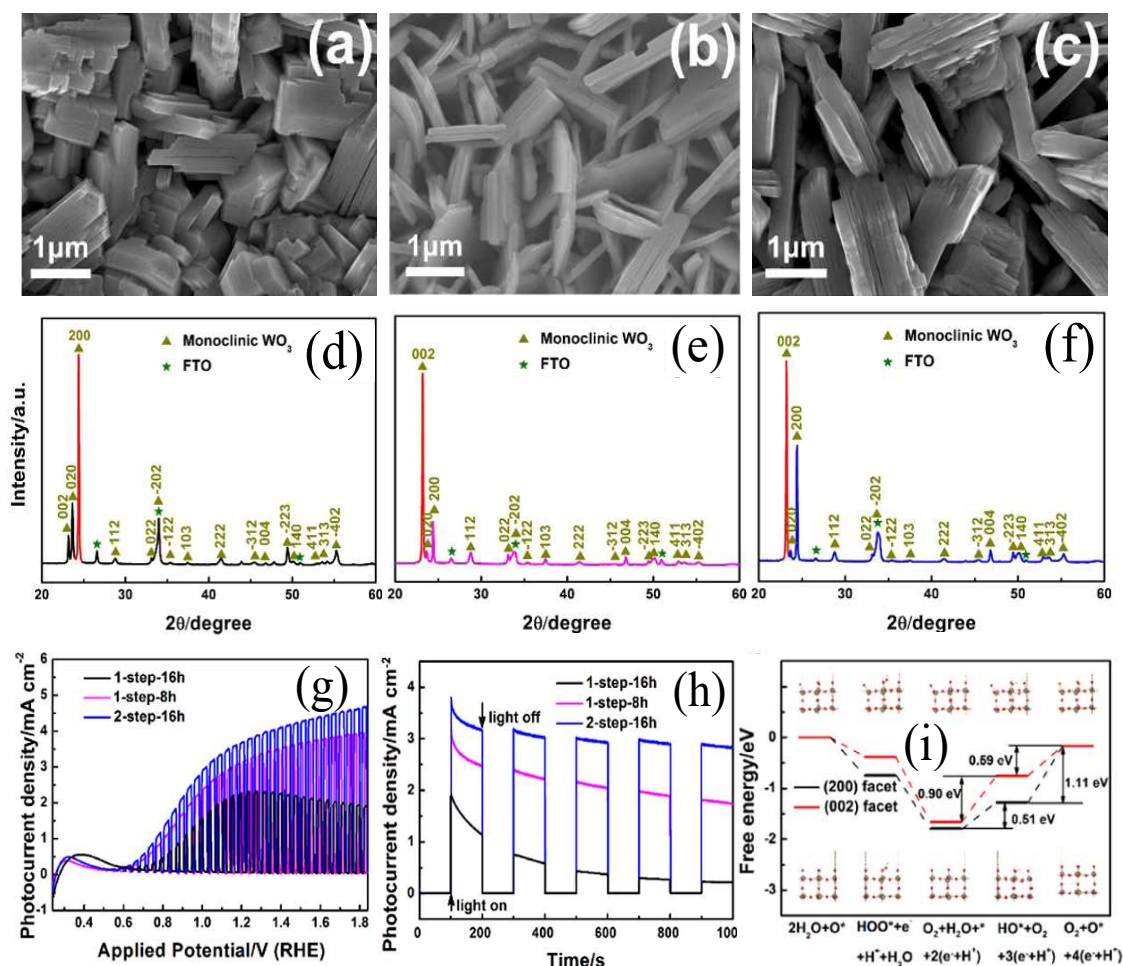
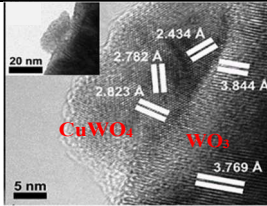
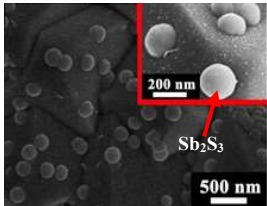
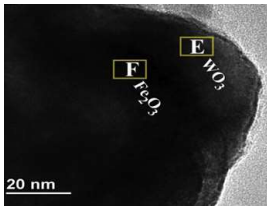
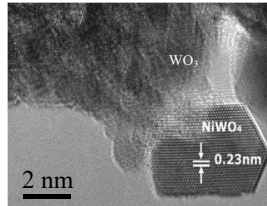
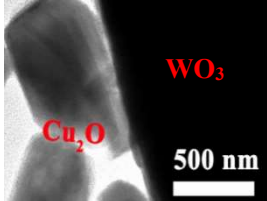


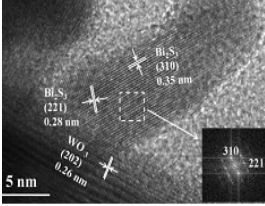
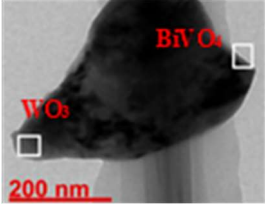
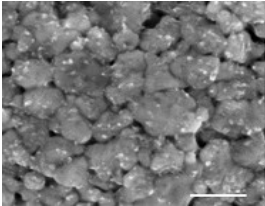
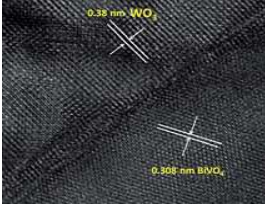
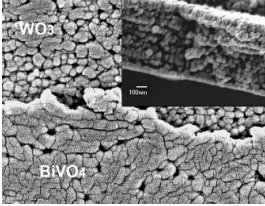
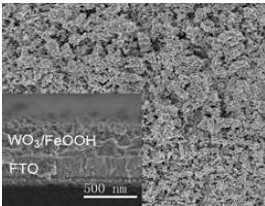
Fig. 6 FESEM images and XRD patterns of (a, d) 1-step-16 h, (b, e) 1-step-8 h, (c, f) 2-step-16 h photoanodes prepared by hydrothermal method, (g) Photocurrent density *vs.* applied potential curves, (h) Photocurrent density *vs.* time measured at 1.23 V *vs.* RHE, and (i) Free energy diagram of the (200) facet and (002) facet at the potential of 1.23 V. Insets: the models that show the surface status of every reaction step: tungsten atoms are represented by gray spheres, oxygen atoms by red spheres, and protons by white spheres, while oxygen gas is not shown in the models. Reproduced from ref. ³² Copyright 2016 Elsevier.

3.4. Forming composites or heterojunctions. Since pristine WO_3 nanomaterials suffer from low solar spectrum absorption (about 12%), slow charge transfer at the electrode/electrolyte interface and rapid electron-hole recombination, it is of great interest to address these problems to improve the photoelectrocatalytic properties of WO_3 by constructing heterojunctions. By connecting two

n-type materials with similar CB and VB energies, one can create a type II heterojunction which can localize electron and hole wave functions in the core or shell material, and thereby improves the charge separation.^{113, 114} Otherwise, coupling n-type semiconductor together with a p-type semiconductor to create p-n junctions¹¹⁵ or Z-scheme system can significantly promote efficient charge separation. To date, a variety of semiconductors are coupled with WO_3 to construct heterojunction, such as $\text{WO}_3/\text{Bi}_2\text{MoO}_6$,¹¹⁶ $\alpha\text{-Fe}_2\text{O}_3/\text{WO}_3$,^{117, 118} $\text{WO}_3/\text{CuWO}_4$,^{85, 119} $\text{NiWO}_4/\text{WO}_3$,¹²⁰ $\text{Bi}_2\text{S}_3/\text{WO}_3$,¹²¹ $\text{WO}_3/\text{BiVO}_4$,¹²²⁻¹²⁵ WO_3/TiO_2 ,^{113, 126} $\text{ZnWO}_4/\text{WO}_3$,¹²⁷ and NiO/WO_3 ,¹²⁸ to enhance the photocatalyst or photoelectric conversion performance. Part of the binary heterojunction, fabrication methods and their PEC water splitting performance are summarized in Table 2. Some ternary heterojunction structures, such as $\text{WO}_3/\text{rGO}/\text{Sb}_2\text{S}_3$,¹²⁹ where rGO serves as the conductive layer, have been reported to enhance the charge transfer. A variety of semiconductors with conduction and valence band energies vs. NHE are shown in Fig. 7a. It is well known that the band gap positions and the Fermi level directly determine the electron transport in the heterostructure systems. In case of WO_3 , coupling with a narrow band gap semiconductor to form a type II heterojunction is an effective way to improve the photocatalytic performance. Normally, the photogenerated electrons could be easily transferred from the CB of the secondary material to the CB of WO_3 while driving photogenerated holes from the VB of WO_3 to the VB of coupled semiconductor which owns a narrower band gap energy (Fig. 7b). Different from the n-type semiconductors where electrons are employed as the photogenerated carriers, the number of holes is much larger than that of electrons for p-type semiconductors. Therefore, in p-n type heterojunction or Z-scheme system, the photo-excited electrons from the CB of WO_3 can readily recombine with the photogenerated holes from the VB of the p-type semiconductor. It is significant to optimize the reduction and oxidation ability for the PEC water splitting (Fig. 7c).

Table 2. Representative WO₃ heterojunction nanostructure for PEC water splitting.

Heterostructure	Fabrication method	SEM/TEM Image	Photoelectrochemistry	Ref
CuWO ₄ /WO ₃	Hydrothermal and then dipping-annealing process		Photocurrent: 1.21 mA cm ⁻² (WO ₃ : 0.64 mA cm ⁻²) at 1.5 V vs. Ag/AgCl; IPCE: 55.3% at ~350 nm at 1.2 V vs. Ag/AgCl; electrolyte: 0.2 M Na ₂ SO ₄	85
WO ₃ /Sb ₂ S ₃	Hydrothermal		Photocurrent: 1.79 mA cm ⁻² at 0.8 V vs. RHE; IPCE: ~12.5% at 300 nm at 0.8 V vs. RHE; electrolyte: 1 M H ₂ SO ₄	39
α-Fe ₂ O ₃ /WO ₃	Hydrothermal and then followed by deposition-annealing		Photocurrent: 1 mA cm ⁻² (WO ₃ : 0.36 mA cm ⁻²) at 1.23 V vs. RHE; IPCE: 30.4% at ~330 nm at 1.23 V vs. RHE; electrolyte: 0.1 M Na ₂ SO ₄	117
NiWO ₄ /WO ₃	Hydrothermal and followed by deposition-annealing		Photocurrent: 0.44 mA cm ⁻² (WO ₃ : ~0.25 mA cm ⁻²) at 1.4 V vs. Ag/AgCl; IPCE: 40.7% at 340 nm at 1.2 V vs. Ag/AgCl; electrolyte: 0.2 M Na ₂ SO ₄	120
WO ₃ /Cu ₂ O	Hydrothermal and then followed electrodeposition		Photocurrent: 1.37 mA cm ⁻² (WO ₃ : 0.39 mA cm ⁻²) at 0.8 V vs. RHE; IPCE: 10.7% at ~300 nm at 0.8 V vs. RHE; electrolyte: 1M H ₂ SO ₄	130

WO ₃ /Bi ₂ S ₃	Hydrothermal and followed by chemical bath deposition		Photocurrent: 5.95 mA cm ⁻² (WO ₃ : 0.17 mA cm ⁻²) at 0.9 V vs. RHE; IPCE: 68.8% at ~435 nm at 0.9 V vs. RHE; electrolyte: 0.1 M Na ₂ S+ 0.1 M Na ₂ SO ₃	131
WO ₃ /BiVO ₄	Soaking hydrothermal-calcining		Photocurrent: 2.92 mA cm ⁻² at 1.81 V vs. RHE; electrolyte: 0.5 M KH ₂ PO ₄	132
WO ₃ /FeOOH	Spray pyrolysis deposition and followed by electrodeposition		Photocurrent: 1.4 mA cm ⁻² (WO ₃ : 0.8 mA cm ⁻²) at 1.23 V vs. RHE; electrolyte: 0.5 M K ₂ SO ₄	133
WO ₃ /BiVO ₄	Hydrothermal and followed by spin coating		Photocurrent: 3.17 mA cm ⁻² (WO ₃ :1.41 mA cm ⁻²) at 1.23 V vs. RHE; electrolyte: 0.1 M Na ₂ SO ₄	134
WO ₃ /BiVO ₄	Solvothermal followed by spin-coating		Photocurrent: 1.6 mA cm ⁻² (WO ₃ : 0.4 mA cm ⁻²) at 1 V vs. RHE; IPCE: 31% at ~420 nm at 0.5 V vs. RHE; electrolyte: 0.5 M Na ₂ SO ₄	135
WO ₃ /FeOOH	Hydrothermal and followed by electrodeposition		Photocurrent: 1.3 mA cm ⁻² (WO ₃ : 0.6 mA cm ⁻²) at 1.23 V vs. RHE; electrolyte: 0.1 M KPi buffer	136

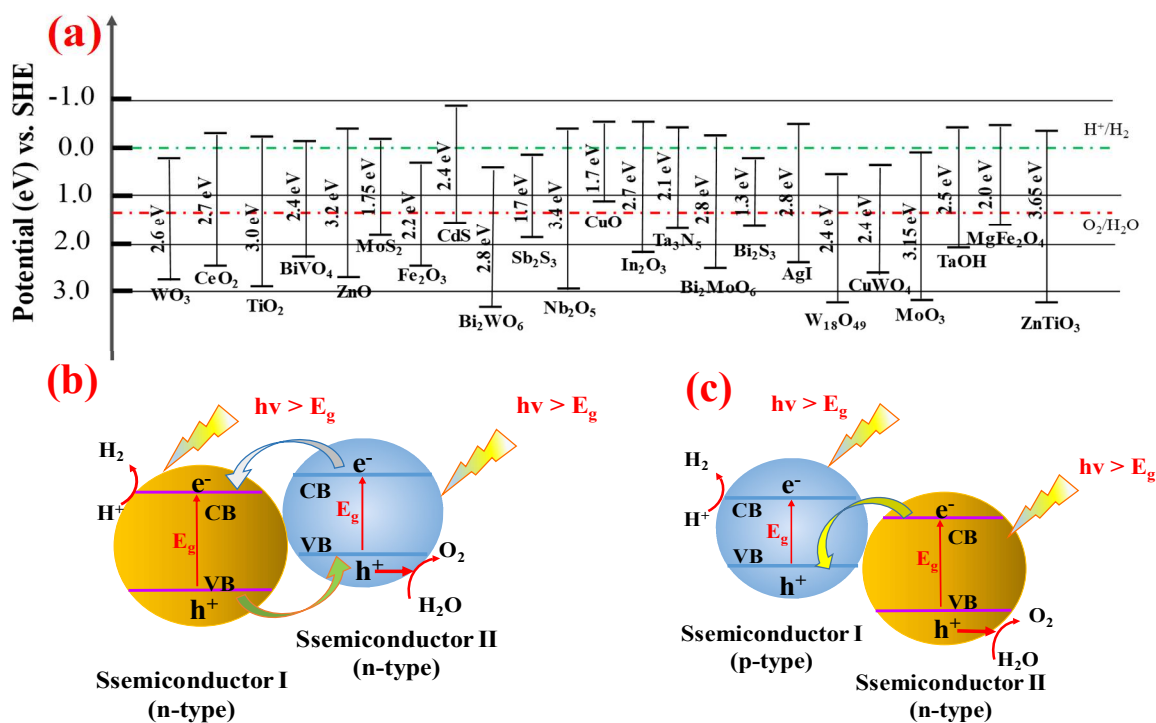


Fig. 7 (a) Bandgap energy, VB and CB positions of several semiconductors on a potential scale (V) vs. NHE/vacuum. (b) Schematic illustration of type II heterojunction and (c) p–n junction band alignments, and the correspondingly possible photoexcited electron-hole pair separation and transfer between the contacted semiconductors.

3.4.1. WO₃/chalcogenide heterojunction. Among various semiconductor materials, narrow bandgap metal sulfides have been widely used as photosensitizers for various wide bandgap semiconductor photoanodes.^{137, 138} As the position of CB and VB of most metal sulfides is more negative than that of WO₃, respectively, coupling of WO₃ with metal sulfide to form heterojunctions is an optimized way to improve the PEC performance. Zhang *et al.* first reported the WO₃/Sb₂S₃ heterojunction photoelectrocatalyst.³⁹ They fabricated three types of WO₃ (WO₃ nanoplates, WO₃ nanorods and WO₃ microcrystals) and their Sb₂S₃ heterojunction photoelectrocatalysts by a facile hydrothermal method. According to UV-vis absorbance spectra and Tauc formula,^{85, 139} the band gaps of WO₃ nanoplates, WO₃ nanorods and microcrystals were

calculated to be 2.96, 2.82, and 2.75 eV, respectively. Meanwhile, the band gaps for the Sb_2S_3 heterojunction were calculated to be 2.75, 2.50 and 2.28 eV, respectively. The decreased band gaps after coupling with narrow band gap Sb_2S_3 indicated the improvement of visible light absorption which could effectively improve the photoelectrocatalytic performance. The $\text{WO}_3/\text{Sb}_2\text{S}_3$ heterojunction could strengthen the migration of charge carrier at the $\text{WO}_3/\text{Sb}_2\text{S}_3$ interface, which in turn effectively facilitated the separation of photogenerated electron-hole pairs. Compared with the pristine WO_3 nanoplates, nanorods and microcrystals, the photocurrent density of the corresponding $\text{WO}_3/\text{Sb}_2\text{S}_3$ heterojunction photoelectrocatalysts was improved by 258%, 308%, and 398%, respectively. Significantly, an excellent and efficient $\text{WO}_3/\text{Bi}_2\text{S}_3$ composites was reported by Wang's group.¹³¹ They designed a 3D WO_3 nanoplate/ Bi_2S_3 nanorod heterostructure photoanode via a hydrothermal process, followed by chemical bath deposition. Based on the UV-vis absorption spectra, the bare WO_3 showed a poor absorption in the visible-light region compared with $\text{WO}_3/\text{Bi}_2\text{S}_3$ heterostructure (the blue plot of Fig. 8b). Moreover, the $\text{WO}_3/\text{Bi}_2\text{S}_3$ heterostructure with a seed layer (the red plot of Fig. 8b) further greatly enhanced the absorption in visible-light light absorption (Fig. 8b). Beneficial for the more negative CB edge of Bi_2S_3 compared to that of WO_3 and excellent contact quality, the photo-excited electrons in the CB of Bi_2S_3 can easily move into the CB of WO_3 and the photo-excited holes in VB of WO_3 will in turn flow to the VB of Bi_2S_3 . This process is significant to enhance the charge transport efficiency, increases the carrier density and reduces the charge recombination, which contributes to the improved PEC activity and stability (Fig. 8a). The as-prepared $\text{WO}_3/\text{Bi}_2\text{S}_3$ composites with a seed layer exhibited an outstanding photocurrent (5.95 mA cm^{-1} at 0.9 V vs. RHE) which is 35 times higher than that of pristine WO_3 (0.17 mA cm^{-1} at 0.9 V vs. RHE). The highest photoconversion

efficiency was increased from 0.03% (at 0.92 V) of the pristine WO_3 to 1.70% (at 0.76 V) of the as-prepared composites (Fig. 8c and d).

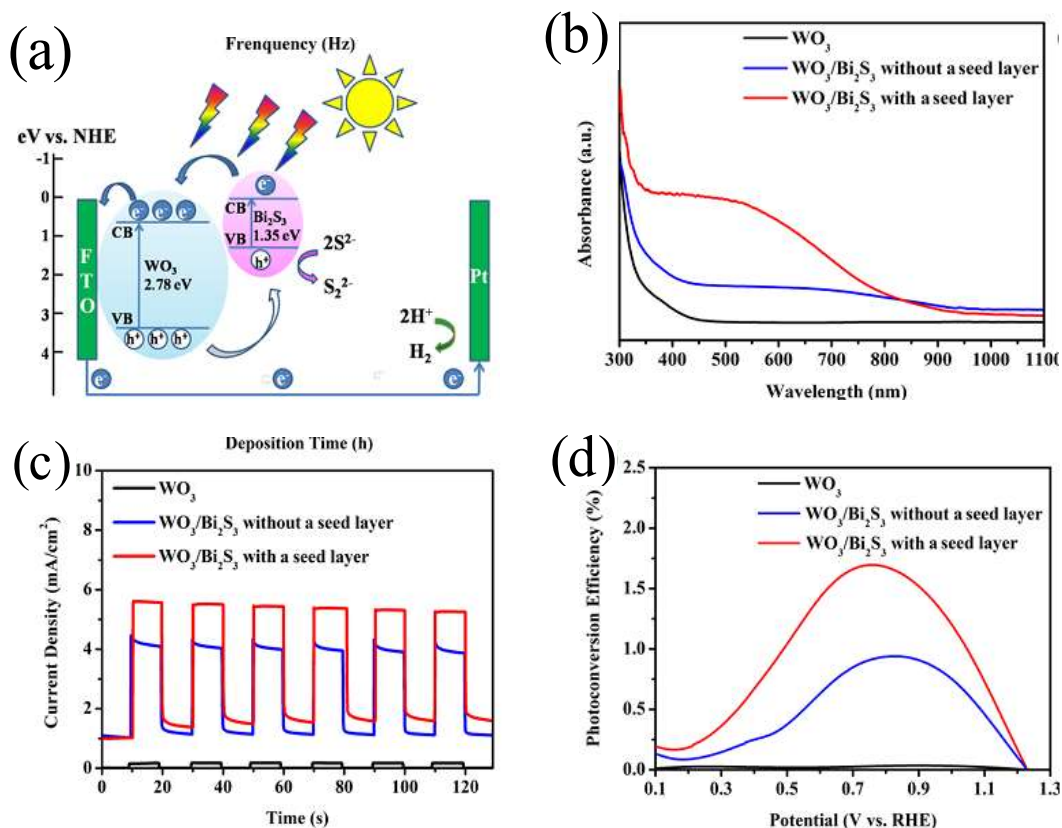


Fig. 8 (a) Schematic of the $\text{WO}_3/\text{Bi}_2\text{S}_3$ heterojunction and the reaction process in the PEC cell, (b) UV-vis absorption spectra of bare WO_3 (black), $\text{WO}_3/\text{Bi}_2\text{S}_3$ without a seed layer (blue) and $\text{WO}_3/\text{Bi}_2\text{S}_3$ with a seed layer (red), (c) I-t curves of bare WO_3 (black), $\text{WO}_3/\text{Bi}_2\text{S}_3$ without a seed layer (blue), and $\text{WO}_3/\text{Bi}_2\text{S}_3$ with a seed layer (red) at 0.9 V vs RHE, (d) Photoconversion efficiency of pristine WO_3 (black), $\text{WO}_3/\text{Bi}_2\text{S}_3$ without a seed layer (blue), and $\text{WO}_3/\text{Bi}_2\text{S}_3$ with a seed layer (red) Reproduced from ref.¹³¹ Copyright 2017 American Chemical Society

3.4.2. $\text{WO}_3/\text{metal oxides heterojunction}$. Although metal sulfide semiconductors have smaller energy gaps, the photocorrosion limits their applications in the photocatalytic water splitting. Therefore, it is a crucial issue to develop a novel narrow bandgap semiconductor with high

photocorrosion resistance. Metal oxides are known to be more stable in various reaction conditions, and consequently it appears to be suitable photocatalysts to couple with WO_3 to construct a heterojunction. For example, Zhang's group achieved a $\text{WO}_3/\text{Cu}_2\text{O}$ heterojunction using an electrodeposition method.¹³⁰ The morphology of as-prepared samples was rod-like (Fig. 9a-b). TEM showed that Cu_2O was evidently deposited onto the surfaces of the WO_3 (Fig. 9c). A series of deposition time were investigated to disclose their impact on PEC water splitting (Fig. 9d). The heterojunction obtained with a deposition time of 240 s exhibited the highest photocurrent density which was attributed to the appropriate amount of Cu_2O nanoparticles that improved both the light absorption and the charge transfer (Fig. 9e). A lower amount of Cu_2O on the surface of WO_3 created a large number of interface defects that intensified the recombination of photogenerated electrons and holes. On the contrary, an excess amount of Cu_2O aroused lattice scattering and decreased the charge carrier concentration, thereby reduced the PEC performance.

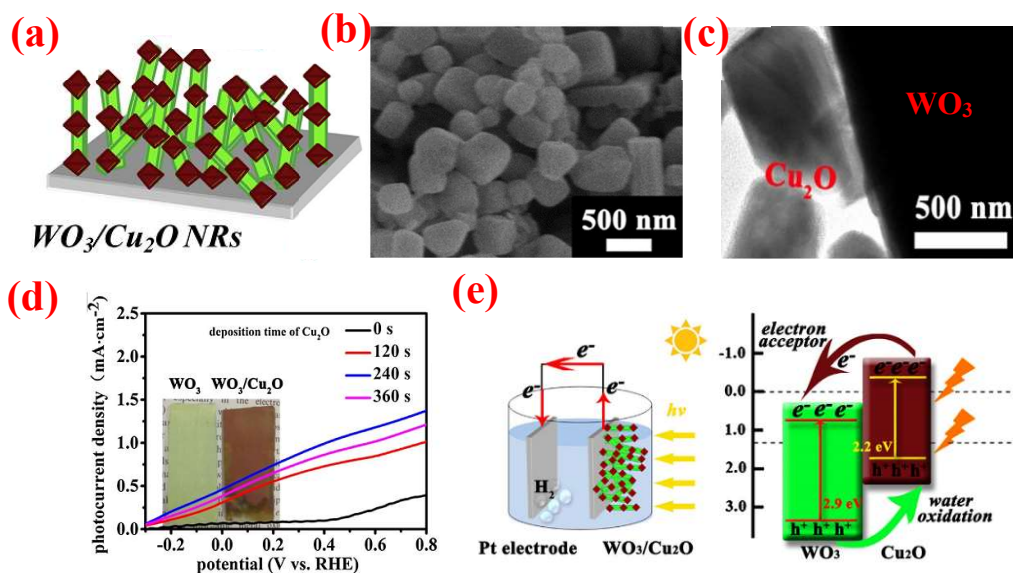


Fig. 9 (a) Schematic of $\text{WO}_3\text{NRs}/\text{Cu}_2\text{O}$ arrays electrodes (b) Typical top view SEM images of $\text{WO}_3\text{NRs}/\text{Cu}_2\text{O}$, (c) TEM images of $\text{WO}_3\text{NRs}/\text{Cu}_2\text{O}$ arrays, (d) The Photocurrent density-voltage curves of the samples, (e) Schematic of the $\text{WO}_3\text{NRs}/\text{Cu}_2\text{O}$ arrays heterojunction photoanode applied in overall water splitting and

simplified schematic illustration of the band-gap energy diagram, showing the enhanced light-harvesting and charge-transfer processes. Reproduced from ref.¹³⁰. Copyright 2017 Elsevier

Zhan *et al.*⁸⁵ fabricated CuWO₄/WO₃ heterojunction photoanodes and demonstrated that coupling with CuWO₄ enhanced the photocurrent density of WO₃ due to the extension of visible light response, efficient separation of photo-excited carriers at the WO₃/CuWO₄ interface and better electron transport properties. The WO₃ decorated with the exfoliated Bi₂MoO₆ nanosheets showed a satisfactory photocurrent density of 2.2 mA cm⁻² at 0.8 V *vs.* SCE compared to WO₃ (1.1 mA cm⁻²). The improved PEC performance of WO₃/Bi₂MoO₆ heterojunction could be attributed to the suitable band position between WO₃ and Bi₂MoO₆ that facilitated the electron-hole separation and charge transfer. The uniformly exfoliated nanosheets coated on the WO₃ surface could also provide a high electric mobility.¹¹⁶

3.4.3. WO₃/BiVO₄ heterojunction. Coating BiVO₄ on the surface of WO₃ to construct a heterojunction could enhance the migration of charge at the interface and significantly increased the light absorption.⁵⁹ BiVO₄ is a highly promising photoanode because of a narrow bandgap of 2.4 eV which leads to the visible light absorption capability, and has an advantageous portion of the CB near the thermodynamic hydrogen evolution potential.¹⁴⁰⁻¹⁴² While the short hole diffusion length and the strong recombination of photoexcited charge carriers limited its performance,¹⁰⁴ it is worth noting that when coupling with BiVO₄ on the surface of WO₃, the photogenerated electrons from the CB of BiVO₄ (+0.02 V *vs.* RHE) can be readily injected into the CB of WO₃ (+0.41 V *vs.* RHE) and the photogenerated holes left in the VB of WO₃ will be transferred to the VB of BiVO₄ due to the matched band edge positions between WO₃ and BiVO₄.^{122, 142-144} This process can effectively promote the separation of photoexcited electrons and holes. In the WO₃/BiVO₄ heterojunction structure, WO₃ mainly acted as electron conductor and BiVO₄ served

as the primary light absorber.^{103, 124, 145, 146} These combined effects could greatly inhibit the recombination of photogenerated electrons and holes, thereby further increases the photoelectric conversion performance.¹³² Served as suitable oxygen evolution catalyst, coupling with BiVO₄ could restrict the formation of peroxy species and increase the stability by blocking the contact of WO₃ and corrosive electrolytes.^{40, 133} Since the first demonstration by P. Chatchai *et al.*,¹⁴⁷ many researchers have paid more attention to improve the PEC activity of WO₃/BiVO₄ heterojunction films.^{103, 104, 122, 123, 142, 146, 134, 135, 148-150} For example, Lee *et al.* emphasized that using highly ordered 1D WO₃ nanostructures with a high aspect ratio and active areas is an effective way to improve the photocatalytic activity of WO₃/BiVO₄ heterojunctions. They compared WO₃/BiVO₄ heterojunction with the same set of WO₃ nanorods and showed that the WO₃/BiVO₄ anodes exhibited higher photocurrent densities than bare WO₃ nanorods.⁵⁹ The WO₃/BiVO₄ heterojunction fabricated by a simple physical deposition and calcination process may cause numerous grain boundaries and increased impedance at the interface of the WO₃/BiVO₄ films.¹⁵¹ Consequently, in-situ synthesis method was preferred to obtain high quality WO₃/BiVO₄ films. For example, Iqbal *et al.*¹⁵¹ synthesized the nanorod-like WO₃/BiVO₄ hetero-nanostructures with a single phase by one step hydrothermal reaction for the first time. In these hetero-nanostructures, BiVO₄ was embedded into the grown nanorods of WO₃. The novel nanorod-like WO₃/BiVO₄ hetero-nanostructure photoanode exhibited a significant photoresponse. In-situ transformed WO₃/BiVO₄ hetero-nanostructures photoanode¹³² exhibited the highest photocurrent density compared to WO₃, BiVO₄, Bi₂WO₆/WO₃ and BiVO₄/WO₃ composites that were prepared via a simple physical deposition. The ratio of BiVO₄ in the WO₃/BiVO₄ hetero-nanostructure influenced the PEC water splitting performance. Seo *et al.*¹⁴⁹ synthesized WO₃/BiVO₄ heterojunctions with various ratios of BiVO₄ and obtained the optimum ratio of complexes. When the concentration of

BiVO₄ was lower, WO₃ was the major photon-absorbing semiconductor and the photogenerated holes could readily recombine at the interface of hetero-nanostructures. While the photogenerated electron-hole pairs were not fully utilized when the thickness of the BiVO₄ layer was larger than 900 nm due to the disappointing charge carrier mobility of BiVO₄. Therefore, the composites with appropriate WO₃ and BiVO₄ exhibited a better PEC water splitting performance.

It is an appealing way to enhance the performance of PEC water splitting by designing special nanostructure semiconductor composites. Core-shell structure is reported to be an efficient system to maximize each separate process optimally which is beneficial for water splitting performance.^{84, 104, 113, 124, 135} By increasing the surface and interface area of the WO₃/BiVO₄ heterojunction, the core-shell heterojunction of WO₃/BiVO₄ promoted the generation and separation of photoexcited electrons and holes. The framework of the core-shell nanostructure can capture multiple reflections of sunlight owing to its cavity which is beneficial for an efficient utilization of solar photons to improve the photocatalytic activity.¹⁴² Therefore, it is critical to develop an optimized WO₃/BiVO₄ core-shell heterojunction to enhance the PEC water splitting properties. Rao *et al.*¹²⁴ synthesized a core-shell structure photoanode incorporated with W-doped BiVO₄ and WO₃. The as-prepared sample exhibited excellent PEC water splitting properties with a high charge separation and surface transfer efficiency. Due to the short hole diffusion length attributed from the core-shell structure, the holes generated in the BiVO₄ shell can readily reach the semiconductor/electrolyte interface and thereby improves the photoelectric conversion efficiency. Jinh's group¹⁴² prepared yolk-shell structured WO₃/BiVO₄ heterojunction with BiVO₄ coating onto the surface and inside of WO₃ shells. As shown in Fig. 10a-f, hollow WO₃ structure, yolk-shell WO₃ spheres and yolk-shell WO₃/BiVO₄ heterojunction were clearly observed. The HR-TEM image (Fig. 10f) and the corresponding energy-dispersive X-ray (EDX) elemental

mapping (Fig. 10g-j) indicated the intimate contact in the $\text{WO}_3/\text{BiVO}_4$ heterojunction structure. Compared with hollow WO_3 , the enhanced photoelectrocatalysts property of the yolk-shell WO_3 was attributed to the particular yolk-shell structure with a beneficial higher charge-carrier separation and a restricted recombination of the photogenerated electrons and holes. After introducing the $\text{FeOOH}/\text{NiOOH}$ layer as oxygen evolution reaction (OER) co-catalyst on the surface of yolk-shell $\text{WO}_3/\text{BiVO}_4$ heterojunction, the composites showed a strong negative shift in the photocurrent onset potential and exhibited the highest photocurrent density (Fig. 10k). In this yolk-shell $\text{WO}_3/\text{BiVO}_4/\text{OER}$ heterojunction, the yolk-shell WO_3 served as electron conductor while BiVO_4 functioned as main light absorber to form type-II heterojunction structure. The photogenerated electrons migrated from the CB of BiVO_4 to the CB of WO_3 . On the other hand, the photogenerated holes left in the VB of WO_3 were injected into the VB of BiVO_4 . This process greatly improved the charge transfer and reduced the recombination of photoexcited electrons and holes. The OER co-catalyst layer reduced the overpotential of water oxidation and subsequently improved the PEC water splitting performance.

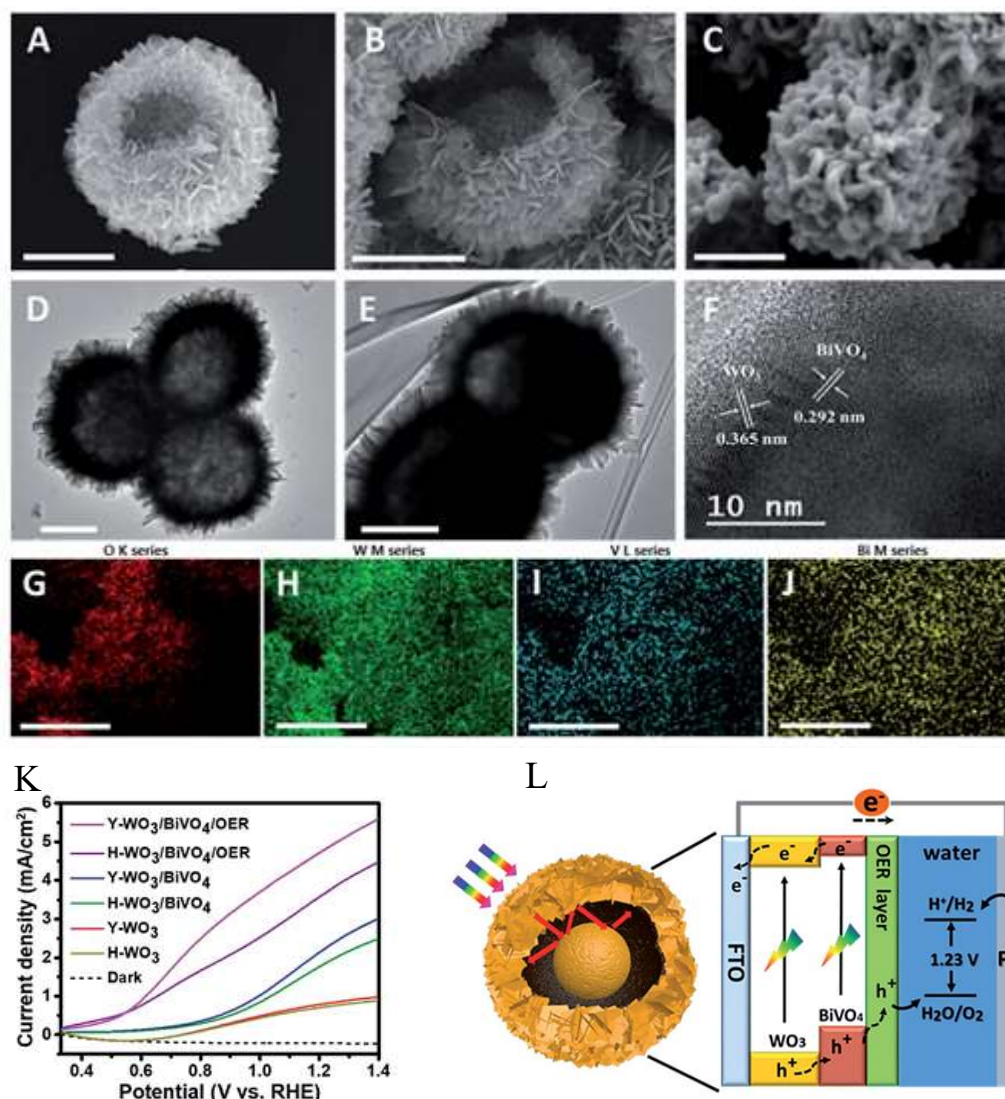


Fig. 10 SEM and TEM images of the hollow WO_3 (A and D) and yolk-shell WO_3 (B and E), (C and F) SEM and HR-TEM images of the yolk-shell $\text{WO}_3/\text{BiVO}_4$ heterojunction, (G–J) The corresponding EDX elemental mapping of the yolk-shell $\text{WO}_3/\text{BiVO}_4$ (scale bars are 1 μm), (K) Linear sweep voltammetry (LSV) curves of the samples in 0.5 M Na_2SO_4 solution under AM 1.5G light illumination, (L) Schematic diagram for the construction of the yolk-shell $\text{WO}_3/\text{BiVO}_4/\text{OER}$ photoanode and the energy diagram for PEC water splitting. Reproduced from ref. ¹⁴². Copyright 2018 Royal Society of Chemistry

3.5. Construction of cocatalysts. 3.5.1. Hydrogen evolution cocatalysts (HEC). To overcome the drawbacks of WO_3 including slow kinetics of OER and rapid recombination of photogenerated

electron-hole pairs, modifying with cocatalysts on the surface of WO_3 is a promising way to increase the efficiency of PEC water splitting.¹⁵² Loading of cocatalysts onto the WO_3 can hinder the charge recombination by providing active sites to facilitate the redox reactions. Cocatalysts increase the trapping sites for the photo-excited electrons and holes, thereby enhance the charge separation and improve the quantum efficiency.^{38, 153, 154} In most cases, noble metals (such as Pd, Pt, Ir, Au, Ag, and Rh) have been employed on the surface of WO_3 as the hydrogen evolution cocatalysts (HEC). When a noble metal is loaded on the surface of WO_3 , a Schottky barrier can be formed. The lower Fermi level of noble metal compared to the WO_3 facilitated noble metal more readily to trap electrons. Thus, the electrons from WO_3 will be injected into the noble metal to equilibrate the Fermi levels. These excessive negative charges in the noble metal and excessive positive charges in WO_3 create a Schottky barrier in the interfaces which can prevent the charge recombination.⁴² The high electron conductivity of noble metal helps to promote the separation of photogenerated electron-hole pairs and enhances the property of water splitting.¹⁵⁵⁻¹⁵⁸ However, the high cost of noble metals limited their large-scale applications. Therefore, low-cost cocatalysts, such as MoS_2 , NiS, WS_2 and C have received more attention during the past few decades.¹⁵⁹⁻¹⁶¹ Among the low-cost HEC cocatalysts, nanocarbon-based cocatalysts have attracted wide attention owing to their high electrical conductivity, large surface area as well as nontoxicity.¹⁶² Shen and coworkers¹⁵⁹ synthesized WO_3 nanoflakes decorated with carbon quantum dots (CQDs) via a solvothermal method followed by subsequent impregnation-assembling. 1.93% CQDs/ WO_3 exhibited an enhanced photocatalytic activity with a photocurrent density of 1.46 mA cm^{-2} at 1.0 V vs. Ag/AgCl, which was about two times higher than bare WO_3 electrode. This enhancement originated from the extended photoresponse range and facilitated charge transfer of CQDs/ WO_3 nanocomposites.

3.5.2 Oxygen evolution cocatalysts (OEC). In overall photocatalytic water splitting, the OER involving a four-electron transfer process is a kinetically slow uphill reaction and becomes the control step for water splitting.^{42, 154, 163} Decorating the oxygen evolution cocatalysts (OEC) with semiconductors can enhance the efficiency of O₂ evolution because the OEC helps to reduce the OER overpotential and suppresses the formation of peroxy species. To load OEC onto WO₃ is thus an effective way to increase the efficiency for water splitting. Thus far, RuO₂,¹⁶⁴ IrO₂,¹⁶⁵ Co-Pi,^{166, 167} Co₃O₄,¹⁶⁸ CoO_x,¹⁶⁹ MnO_x,¹⁷⁰ and NiO_x¹⁷⁰ have served as OEC for the photocatalytic O₂ production. Amongst, Co-Pi has received much attention due to its outstanding OER performance.^{171, 172} Seabold and co-workers⁴⁰ coupled WO₃ with a layer of Co-Pi to improve the photostability of WO₃ photoanodes and enhanced the photo-oxidation reaction. After photocurrent measurement for 2 h, the appearance of pores and the decrease of crystal grains of WO₃ electrode indicate that OER is not the sole photo-oxidation reaction occurring at the bare WO₃ electrode. Peroxy species at the WO₃ surface were formed resulting in a loss of PEC activity of bare WO₃ electrode. After the deposition of Co-Pi OEC layer on the WO₃ electrodes, the photocurrent remained stable over long time since Co-Pi OEC effectively inhibited the formation of peroxy species at the surface and prevented the photochemical deactivation of the WO₃. Fan *et al.*⁷⁷ proposed a rational design via combining WO₃ and NiFe-layered double hydroxide (LDH) nanoarrays. The WO₃ nanorod arrays were prepared via a hydrothermal process and decorated with NiFe-LDH by the electrochemical deposition (Fig. 11a-c). They found that the deposition time of NiFe-LDH significantly affected the PEC performances and obtained the best performance measured for the WO₃@NiFe-LDH-200s sample. The as-prepared sample exhibited excellent photocurrent density and higher stability compared with bare WO₃ nanorods (Figure 11d). As an efficient OER catalyst, the NiFe-LDH could effectively facilitate the separation of photogenerated

electron-hole pairs and enhanced water splitting kinetics. After coupling with NiFe-LDH, the photoexcited holes in WO_3 preferentially oxidized the low valence Ni^{II} in the redox couples of LDH to the high valence $\text{Ni}^{\text{III,IV}}$, and then the high valence $\text{Ni}^{\text{III,IV}}$ further oxidized water to release oxygen. This oxidation process has been demonstrated to be kinetically faster than water oxidation directly via photogenerated holes (Fig. 11e). As the promotion of water splitting kinetics and hindering the charge recombination, the $\text{WO}_3@$ NiFe-LDH-200s sample exhibited a superior PEC water oxidation performance. However, a thick OEC layer inevitably blocked the incident light and reduced the PEC activity of WO_3 .^{32, 40} It is highly desirable to improve the stability of the WO_3 photoanode without sacrificing the photocatalytic activity.

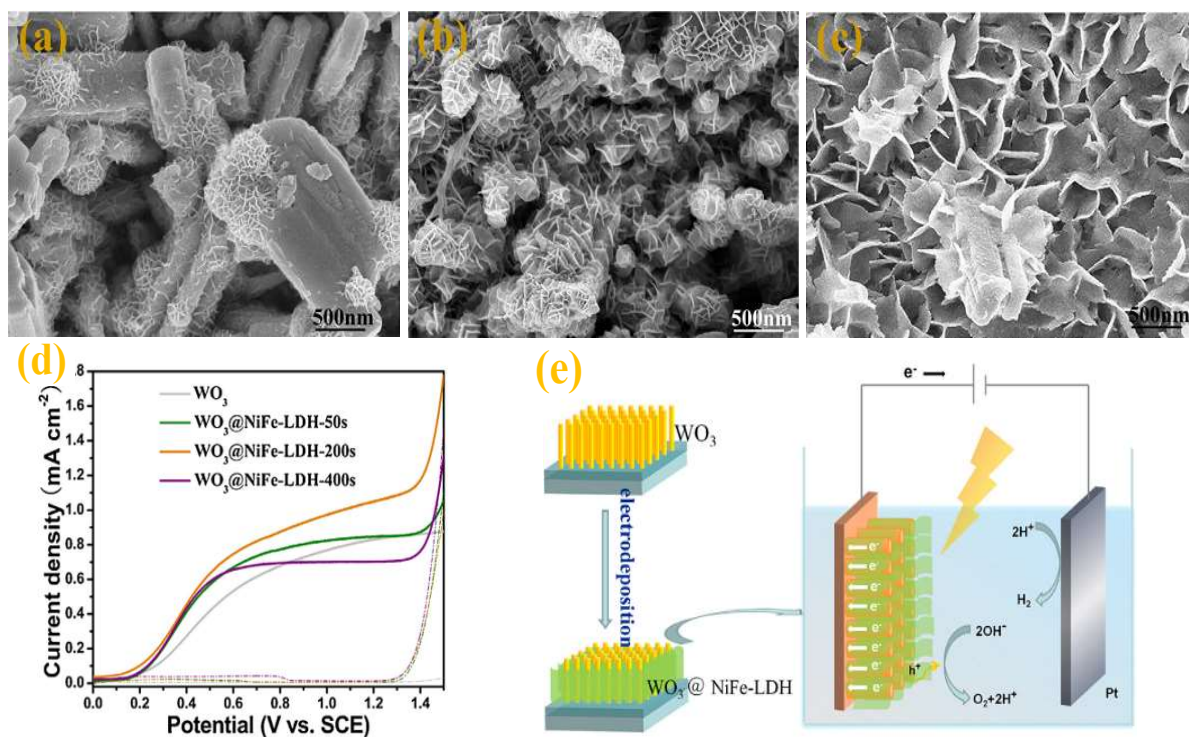


Fig. 11 SEM images of $\text{WO}_3@$ NiFe-LDH NR arrays obtained with various electrodeposition durations: (a) 50 s, (b) 200 s, (c) 400 s, (d) Linear sweep voltammograms at a scan rate of 10 mV s^{-1} (solid line: under visible light, dashed line: in dark) and (e) PEC water oxidation mechanism on the $\text{WO}_3@$ NiFe-LDH NR arrays under visible light. Reproduced from ref. ⁷⁷ Copyright 2016 Elsevier.

3.6. Doping or oxygen deficiency. There exist two main kinds of defects in WO_3 . One is oxygen deficiency, which accelerates the charge carrier transfer at an optimized amount.^{173, 174} The other is the trap states that promote the recombination of electrons and holes. Serving as shallow donors, the bulk oxygen vacancies can improve electrical conductivity and facilitate charge transfer, while surface oxygen vacancies introduce a large number of defects which can be the center of recombination of photogenerated electron-hole pairs and thereby reduces the PEC performance.³⁸ Therefore, it is one of the key objectives to reduce the surface oxygen vacancies without affecting the bulk oxygen vacancies. Li *et al.* synthesized a series of substoichiometric WO_{3-x} nanoflakes and demonstrated that the enhanced photocurrent density was related to the increased donor density after introducing oxygen vacancies. The observed anodic shift of the hydrogen-treated samples was due to excessive surface oxygen vacancies which aggravated the charge carrier recombination.³³ Li *et al.* introduced oxygen vacancies by adding TiCl_3 . They demonstrated that the oxygen vacancies were introduced in a proportion to the concentration of TiCl_3 . Treatment by TiCl_3 at high concentration led to excessive surface oxygen vacancies that resulted in a thicker disorder layer with more recombination centers.¹⁷⁵ Similar results were obtained by the treatment of WO_3 via H_2O_2 to introduce surface oxygen vacancies.¹⁷⁶ Gong *et al.*⁶⁷ synthesized WO_3 nanoflakes photoanode with decreased surface oxygen vacancies but suitable bulk oxygen vacancies by a facile hydrogen annealing followed by an ozone treatment (named as HO- WO_3). The remarkable enhancement in the photocurrent values from 1.09 mA cm^{-2} for pristine WO_3 to 2.25 mA cm^{-2} for the HO- WO_3 sample at 1.23 V vs. RHE was achieved. The improved performance of the HO- WO_3 sample was due to the increased bulk oxygen vacancies that served as shallow electron donors to enhance the conductivity of WO_3 and the decreased surface oxygen vacancies that reduced the recombination of photogenerated electrons and holes. However, the

introduction of oxygen vacancies using hydrogen treatment resulted in high consumption of hydrogen gas, which hindered their applications in practical fields.

Concerning the traps, modifying the passivation layer on the surface of semiconductor particles can inhibit the recombination of photogenerated electrons and holes. Doping with a hetero-element can extend the photoresponse range and increase the carrier concentration. However, due to different radii between the donor atom and the host atom, the introduction of dopant will cause a significant increase of lattice distortion and thus results in the increase of carrier recombination centers.¹⁷⁷⁻¹⁷⁹ Doping with a hetero-element will decrease the solubility of dopant species and reduce the structural stabilities.^{179, 180} Therefore, it is the most critical issue to select the optimized doping element leading to an inconspicuous structural disturbance and sparse defect sites. Transition metals and lanthanides are able to intercept the electronic structure of WO_3 to extract more visible solar spectra.¹⁸¹ Doping Ti^{4+} into the WO_3 semiconductor is a feasible way to improve the PEC performance because impurity states between the CB and VB of WO_3 change the band structure of WO_3 . Meanwhile, similar radii of the guest and the host result in less lattice distortion.¹⁸² Yb, as one of lanthanides, is an electron-rich f-orbital element which increases the charge carrier generation for the enhanced photocurrent densities in WO_3 . Liew *et al.*¹⁸¹ synthesized Yb-doped WO_3 photocatalysts by the method of co-sputtering of WO_3 and Yb. They demonstrated that the samples prepared under W and Yb sputtering powers of 100 W and 5 W, respectively, exhibited the highest photocurrent density. As the ionic radius of Yb^{3+} is 28% larger than that of W^{6+} , it is easier for Yb^{3+} to contribute electrons from its outer shell $4f^{13}$ to the conductive carrier path in WO_3 which is beneficial for reducing the charge transfer resistances and enhancing the efficiency of charge transfer at the photocatalyst/electrolyte interface. Nevertheless, excessive Yb^{3+} caused higher densities of grain boundary which acted as carrier recombination

centers to reduce the hole-electron separation efficiency. Other metals, such as Bi,¹⁸³ Al,¹⁸⁴ Ni,¹⁸⁵ Co,¹⁸⁶ and Mo¹⁸⁷ were employed as dopants for WO₃ to enhance the PEC water splitting performance. Since the introduction of metal element into semiconducting oxides reduced the thermal stability, doping of nonmetal elements has attracted considerable attention.¹⁸⁸ Doping N into WO₃ significantly narrowed the band gap of WO₃ to a value lower than 2.0 eV and thereby greatly enhanced the photo absorption performance.¹⁸⁹ In S-doped WO₃, some S atoms replaced O atoms on the surface of WO₃ and some S⁶⁺ more favorably substituted W⁶⁺ to form W-O-S bonds.¹⁹⁰ Oxygen vacancies increased to reduce the resistivity and increased the extrinsic absorption. Thus, it significantly increased the absorption of visible light and enhanced the PEC water splitting performance. Despite doping is an effective strategy to introduce oxygen vacancies and enhances the visible light absorption, doping with hetero-element resulted in a highly defective lattice and seriously limited their practical applications.

4. Z-Scheme water splitting

Although coupling with other n-type semiconductors to form II heterojunctions can significantly improve the photocatalytic performance of WO₃, to achieve overall water splitting is limited without changing the original oxidation and reduction potential. Recently, inspired by natural photosynthesis in green plants, great attention has been paid to construct Z-scheme heterojunctions for the overall water splitting under visible light irradiation due to their efficient photogenerated electron-hole separation and optimized redox ability of the photocatalytic system.¹⁹¹⁻¹⁹⁴ Yousaf *et al.*¹⁹⁵ constructed efficient Z-scheme junctions consisting of oxygen-deficient WO_{3-x} nanorods and Zn_{0.3}Cd_{0.7}S nanoparticles and found that H₂ was produced in a repeatable manner from aqueous solutions containing Na₂SO₃ and Na₂S as sacrificial reagents without electric energy. Zhu *et al.*¹⁹⁶ prepared carbon nanodots (CNDs) from glucose via a simple hydrothermal process and found that

the CNDs without any modification and doping could produce relatively low hydrogen under xenon lamp irradiation. More importantly, after combined with WO_3 to form Z-scheme through an IO_3^-/I^- shuttle redox mediator, the H_2 evolution rates of the as-prepared CNDs/ WO_3 Z-scheme reached up to $1330 \mu\text{mol g}^{-1}\text{h}^{-1}$, which was about 286 times higher than that of pure CNDs.

Although the more positive VB than the oxygen generation potential makes WO_3 suitable for oxidizing water to generate oxygen, the positive position of CB limits the reduction of H^+ to H_2 . Thus, WO_3 cannot be used for overall water splitting. A strategy to overcome the inherent limits is to introduce Z-scheme junctions to produce hydrogen from water splitting. The fundamental principle of the Z-scheme water splitting is shown in Fig. 12a. In this system, semiconductor I with the CB more negative than the hydrogen generation potential is combined with semiconductor II with the VB more positive than the oxygen generation potential through an appropriate shuttle redox mediator. Compared with one-step water splitting systems, Z-scheme junctions utilize visible light more efficiently due to the reduced energy required to drive each photocatalyst. It is thus possible to apply a photocatalyst that has either a water reduction or oxidation potential to one side of the system. A reversible redox mediator, noble metal particle or graphene has been used as the shuttle electron mediator. Till now, there have been many reports on the Z-scheme junctions with an appropriate shuttle redox mediators for overall water splitting.¹⁹⁷⁻¹⁹⁹ Whereas, many problems exist for the Z-scheme photocatalysts with shuttle electron mediators in water splitting, such as the complicated synthesis process, strong photocatalytic backward reaction and the spectral shielding effect by the shuttle redox mediators.²⁰⁰⁻²⁰²

In the past few decades, direct Z-scheme has attracted great attention due to its simple synthesis and wide range light absorption. A schematic illustration of WO_3 based direct Z-scheme

junctions is shown in Fig. 12b. Both the CB and the VB of the coupled semiconductors are higher than those of WO_3 . The CB position of coupled semiconductor is higher than the position of $2\text{H}^+/\text{H}_2$. Meanwhile, a great quantity of defects could be readily accumulated at the solid–solid heterointerface, which possesses some similar properties to those of a conductor such as analogous energy levels and low electric resistance. These features prompt the interface to be apt to serve as a recombination center of e^-h^+ pairs.²⁰³ Therefore, the photoexcited electrons with a lower reduction ability migrated from the CB of WO_3 to recombine with the photogenerated holes with a lower oxidation ability in the VB of coupled semiconductor. The left photogenerated electrons and holes are able to keep strong redox states, which are promising for the overall water splitting. It is worth noting that compared to type II heterojunction, the charge carrier migration is more feasible for the direct Z-scheme photocatalyst that is attributed to the electrostatic attraction between the electrons and holes. Therefore, photogenerated electron-hole pairs are more readily separated in the Z-scheme heterojunctions, and hence the recombination will be significantly suppressed.

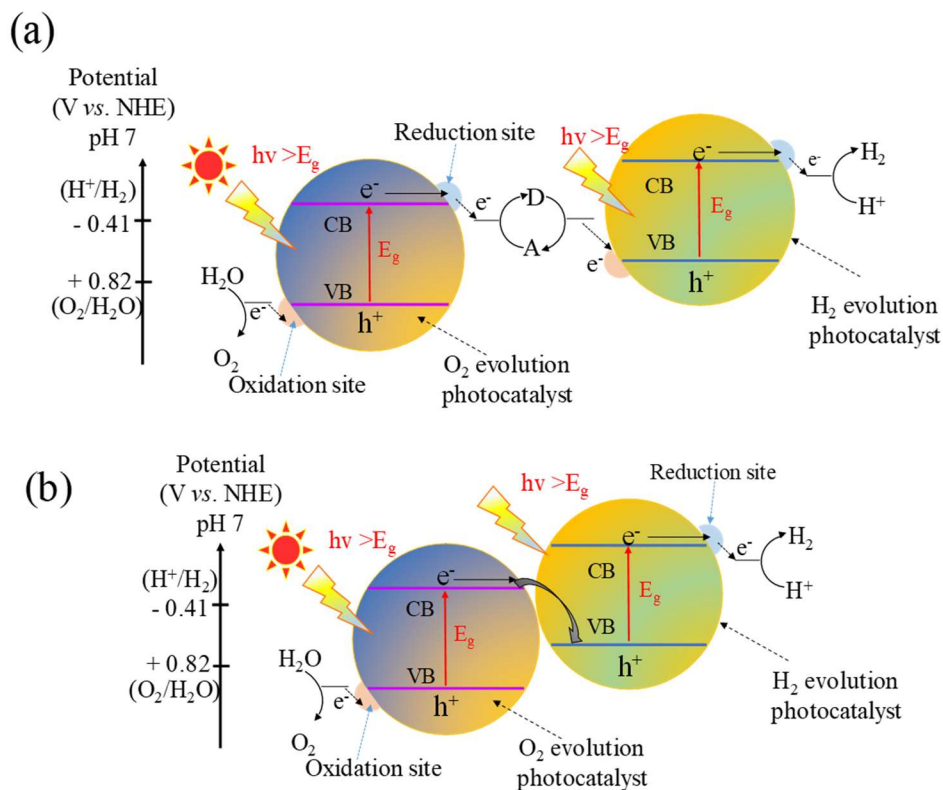


Fig. 12 Schematic illustration of (a) Z-scheme junction band alignments with an appropriate shuttle redox, (b) Direct Z-scheme without electron mediator for overall water splitting. CB, conduction band; VB, valence band; E_g, band gap.

Electron spin resonance (ESR) spin-trapping technique with DMPO under visible light illumination is an effective method to confirm the reaction mechanism of the electron–hole separation in the Z-scheme system. Generally, the CB potential of WO₃ located at ~ 0.71 eV vs. NHE is more positive compared with the reduction potential of active superoxide ($\cdot\text{O}^{2-}$) ($\text{O}_2/\cdot\text{O}^{2-} = -0.284$ eV_{NHE}). Thus, the photo-generated electrons on the surface of the WO₃ are thermodynamically unable to react with O₂ to produce $\cdot\text{O}^{2-}$. In other words, negligible signals of DMPO– $\cdot\text{O}^{2-}$ can be found for pure WO₃. Whereas WO₃ can exhibit a clear DMPO– $\cdot\text{OH}$ signal which is ascribed to the more positive VB potential compared with the oxidation H₂O/or OH⁻ to the $\cdot\text{OH}$ radicals ($\text{OH}^-/\cdot\text{OH} = +2.4$ eV). Xiao *et al.*^[194] introduced g-C₃N₄ to combine with WO₃ to

form Z-scheme nanojunction. They found that the DMPO- $\cdot\text{O}^{2-}$ signal was only observed over $\text{WO}_3/\text{g-C}_3\text{N}_4$ and $\text{g-C}_3\text{N}_4$ and the DMPO- $\cdot\text{OH}$ signal was only observed over $\text{WO}_3/\text{g-C}_3\text{N}_4$ and WO_3 . This result implies that both $\cdot\text{O}^{2-}$ radicals and $\cdot\text{OH}$ radicals can generate over $\text{g-C}_3\text{N}_4/\text{WO}_3$ heterostructures, whereas WO_3 can only produce the $\cdot\text{O}^{2-}$ radicals and $\text{g-C}_3\text{N}_4$ can only generate the $\cdot\text{OH}$ radicals. Therefore, in the $\text{g-C}_3\text{N}_4/\text{WO}_3$ Z-Scheme system, electrons on the CB of $\text{g-C}_3\text{N}_4$ remain a high reduction capability to reduce O_2 to the $\cdot\text{O}^{2-}$ radicals as well as the holes on the VB of WO_3 still keep sufficient high oxidation capability to oxidize H_2O /or OH^- to the $\cdot\text{OH}$ radicals.

Xie *et al.*²⁰⁴ constructed a CdS/WO_3 Z-scheme nanojunction with lactate as the electron donor. The optimized CdS/WO_3 Z-scheme nanojunction showed a high rate of H_2 evolution without electric energy, which was four times higher than CdS . WO_3 exhibited no H_2 production performance. The amount of CdS on the surface of WO_3 had a significant effect on the property of the Z-scheme nanojunction, that is, high amount of CdS hindered the WO_3 from absorbing light and generated the recombination center of photogenerated charges, which reduced the photocatalytic activity. After introducing Pt as the cocatalyst to improve the charge transport between CdS and WO_3 , H_2 evolution rates increased up to $2900 \mu\text{mol g}^{-1}\text{h}^{-1}$ under a visible radiation, which was about 7.9 times higher than that of the as-prepared CdS/WO_3 Z-scheme nanojunction under visible light irradiation. Dai *et al.*²⁰⁵ introduced diethylenetriamine (EDTA) as structure-directing agents and designed a direct Z-scheme system of $\text{WO}_3/\text{CdS-EDTA}$ composites to achieve an overall water splitting without using electric energy. A distinct separation of electrons and holes was observed in the Z-scheme structure, in which the photo-excited electrons in the CB of WO_3 recombined with the photo-excited holes in the VB of CdS . This in turn avoided the enriching of holes on the VB of CdS which effectively reduced the photocorrosion of CdS as well as improved the PEC performance.

Graphitic carbon nitride (g-C₃N₄) is an organic semiconductor, and it has been intensively studied as a novel metal-free photocatalyst owing to its visible-light absorption, narrow band gap, high reduction ability and high chemical stability.²⁰⁶⁻²⁰⁸ The CB edge potential of g-C₃N₄ (-1.13 eV)²⁰⁹ is more negative than the potential of 2H⁺/H₂ (-0.41 V vs. NHE at pH 7),²¹⁰ indicating that H₂ can be produced on the surface of g-C₃N₄. In contrast to WO₃, O₂ could not be generated on the surface of g-C₃N₄ because of the more negative VB edge potential (~1.57 eV)²⁰⁹ than the potential of H₂O/O₂ (0.82 V vs. NHE).²¹⁰ The suitable band gap of CB and VB between WO₃ and g-C₃N₄ offers appropriate driving forces to separate and transfer photogenerated electron-hole pairs and makes it possible to structure Z-scheme semiconductor nanocomposites. Therefore composite structure is expected to improve the photocatalytic activity of WO₃ by increasing the number of photogenerated charge carriers. In recent years, constructing the Z-scheme WO₃/g-C₃N₄ composites has been reported for the complete oxidation of organic compounds or overall water splitting.²¹¹⁻²¹⁴ In Xiao's work,²¹⁵ Z-scheme WO₃/g-C₃N₄ composites with hollow microspheres were fabricated by in situ hydrolysis and a polymerization process consecutively. The prepared heterojunction contains numerous interfaces and highly exposed oxidation-reduction active sites. Due to the unique Z-scheme architecture, more incident photons are expected to be trapped in the hollow cavities, and thus contribute to more electrons and holes available for photocatalytic reactions. The photoluminescence (PL) decay profiles show that a prolonged lifetime of ~2.23 ns for the WO₃/g-C₃N₄ compared to ~1.62 ns for the bare WO₃ improved the reaction abilities and significantly enhanced the photocatalytic efficiency of WO₃/g-C₃N₄. Cui *et al.*²¹⁶ prepared direct Z-scheme WO₃/g-C₃N₄ composites via a facile one-step heating procedure, which exhibited an improved photocatalytic activity. Complexing WO₃ with g-C₃N₄ caused the red shift which promoted the separation of photogenerated electron-hole pairs. Lu and co-workers²¹⁷ established

a system by combining WO_3 and $\text{g-C}_3\text{N}_4$. This system showed an enhanced photocurrent compared to pure WO_3 , which was ascribed to the accelerated charge separation in the heterointerface because of the optimal structure of the direct Z-scheme. Zhao and coworkers²⁰⁹ combined C_3N_4 and WO_3 to form a direct Z-scheme system via a facile hydrothermal method. In this Z-scheme system, accompanied with 1 wt% Pt, H_2 and O_2 were generated as much as 30.3 and 14.8 mmol after 20 h visible light irradiation ($\lambda > 420$ nm), while trace amounts of H_2 and O_2 were detected over pure $\text{g-C}_3\text{N}_4$. After introducing rGO as electron mediator to generate ternary composites, the as-prepared samples were able to release hydrogen and oxygen under a visible light irradiation with a relatively high performance. The apparent quantum yield efficiency of the well-prepared ternary composites was *ca.* 0.9% while the homologous sample without rGO showed a smaller value (*i.e.*, 0.7%) under a monochromatic light at 420 nm. Due to its excellent conductivity, rGO promoted the photoexcited electrons transfer from WO_3 to the photo-generated holes in C_3N_4 , acting as a promising electron mediator. Peng *et al.*²¹⁸ designed a direct Z-scheme $\text{g-C}_3\text{N}_4/\text{WO}_3$ photocatalyst via partial intercalation of the WO_3 within $\text{g-C}_3\text{N}_4$ to enhance the activities of photocatalytic H_2 production. The scanning transmission electron microscopy (STEM) clearly resolved the well-defined interfaces between $\text{g-C}_3\text{N}_4$ and WO_3 , which prompted the charge transportation and benefited the recombination of electrons in the CB of WO_3 and holes in the VB of $\text{g-C}_3\text{N}_4$. The internal electric field was suggested to provide the force to drive the Z-scheme electron transportation at the interfacial junction. This increased the lifetime of excited electrons in $\text{g-C}_3\text{N}_4$ and excited holes in WO_3 , therefore, enhanced the photocatalytic efficiency for the overall water splitting.

5. Summary and outlook

Photoelectrochemical water splitting to generate H_2 is a promising approach for our future energy sustainability and has attracted remarkable attention in the past decade. Challenges facing today are to develop photoanodes with high efficiency, stability, and low cost in practical applications. WO_3 is one of the promising materials for its visible light response, durable and efficient operation in aqueous solution. Boosting the PEC water splitting performance of WO_3 can be achieved with managing morphology, crystallinity, heterojunction, oxygen vacancy, doping, and co-catalysts. Compared to bulk structures, nanostructures are of great interest in absorbing more photons and consequently improved the photoelectric conversion efficiency. In particular, 2-D nanostructure with more significant surface/volume ratios is favorable for highly efficient and directional transport of electrons and holes, thus promoting the electron transfer to the back-contacted conductive substrate. Concerning the crystal structure, tremendous researches have proved that the monoclinic phase of WO_3 is the most stable phase at room temperature and more active for OER compared with the hexagonal or orthorhombic phases of WO_3 . Highly reactive (002) facets promote the consumption of photo-excited holes to split the adsorbed water molecules into hydrogen, hinder the recombination of photogenerated electron-hole pairs and suppress the formation of peroxo species to maintain the stability of WO_3 .

To solve the drawbacks of pristine WO_3 with a slow charge transfer at the electrode/electrolyte interface and a rapid electron-hole recombination, coupling with narrow band gap semiconductor to create a type II heterojunction is an effective strategy to separate photogenerated hole–electron pairs and to enhance the efficiency of PEC water splitting. Adding optimized amount of oxygen deficiency in the catalyst can accelerate the charge carrier transfer and impede the charge carrier recombination. Doping with hetero-elements can extend the photo response range and increase the carrier concentration. Decorating with co-catalysts helps for

improving the surface kinetics and reducing the oxygen evolution overpotential that suppresses the formation of peroxy species.

The less negative CB of WO_3 compared to the potential of hydrogen generation makes it unsuitable for overall water splitting. A strategy to overcome this inherent limit is to introduce Z-scheme junctions to produce H_2 from water splitting, which not only significantly facilitates the separation of electrons and holes but also keeps the photogenerated electrons and holes in the strong redox states.

Although tremendous efforts have been made to synthesize modified nanostructured WO_3 or their composites, the PEC water splitting efficiency still fails to meet industrial applications. Researchers ignored that WO_3 is only stable in acidic media of pH lower than 4 according to the Pourbaix diagrams, and thus future researches have to investigate the PEC performance of WO_3 under strong acidic conditions. The theoretical research of WO_3 in PEC process should be taken into account to deeply understand the underlying physics and chemistry. Otherwise, many on-going challenges in improving the stability of WO_3 and preventing the rapid recombination of electrons and holes should be solved to improve the PEC water splitting performance in the near future.

Acknowledgments

This work was supported by Beijing Natural Science Foundation (2151001, 2154043), National Natural Science Foundation (51534009, 52621003, 51402008), Scientific Research Project of Beijing Municipal Education Commission (KM201610005026) and the New Century National Hundred, Thousand and Ten Thousand Talent Project and Beijing municipal high-level innovative team building program (No. IDHT 20170502). Q.G. was supported as part of the Fluid Interface Reactions, Structures and Transport (FIRST) Center, an Energy Frontier Research Center funded

by the U.S. Department of Energy, Office of Science, Office of Basic Energy Sciences. A portion of this research was conducted at the Center for Nanophase Materials Sciences, which is a DOE Office of Science User Facility.

References

- 1 (a) D. M. Fabian, S. Hu, N. Singh, F. A. Houle, T. Hisatomi, K. Domen, F. E. Osterloh and S. Ardo, *Energy Environ. Sci.*, 2015, **8**, 2825–2850; (b) R. Li, X. Zhu, Q. Fu, G. Liang, Y. Chen, L. Luo, M. Dong, Q. Shao, C. Lin, R. Wei and Z. Guo, *Chem. Commun.*, 2019, **55**, 2493–2496; (c) C. Hou, J. Wang, W. Du, J. Wang, Y. Du, C. Liu, J. Zhang, H. Hou, F. Dang, L. Zhao, and Z. Guo, *J. Mater. Chem. A*, 2019, **7**, 13460–13472; (d) Y. Liu, M. Shi, C. Yan, Q. Zhuo, H. Wu, L. Wang, H. Liu and Z. Guo, *J. Mater. Sci.*, 2019, **30(7)**, 6583–6592; (e) L. Yang, M. Shi, J. Jiang, Y. Liu, C. Yan, H. Liu and Z. Guo, *Mater. Lett.*, 2019, **244**, 27–30; (f) M. Liu, Z. Yang, H. Sun, C. Lai, X. Zhao, H. Peng, T. Liu, *Nano Res.* 2016, **9**, 3735–3746; (g) M. Liu, B. Li, H. Zhou, C. Chen, Y. Liu, T. Liu, *Chem. Commun.* 2017, **53**, 2810–2813; (h) J. Cai, W. Xu, Y. Liu, Z. Zhu, G. Liu, W. Ding G. Wang, H. Wang, Y. Luo, *Eng. Sci.*, 2019, **5**, 21–29; (i) W. Zhao, X. Li, R. Yin, L. Qian, X. Huang, H. Liu, J. Zhang, J. Wang, T. Ding, and Z. Guo, *Nanoscale*, 2019, **11**, 50–59.
- 2 (a) Z. G. Zou, J. H. Ye, K. Sayama and H. Arakawa, *Nature*, 2001, **414**, 625–627; (b) M. Liu, Q. Meng, Z. Yang, X. Zhao, T. Liu, *Chem. Commun.*, 2018, **54**, 5090–5093; (c) M. Liu, Y. Liu, Y. Yan, F. Wang, J. Liu, T. Liu, *Chem. Commun.* 2017, **53**, 9097–9100; (d) Q. Hu, N. Zhou, K. Gong, H. Liu, Q. Liu, D. Sun, Q. Wang, Q. Shao, H. Liu, B. Qiu and Z. Guo, *ACS Sustain. Chem. Eng.*, 2019, **7**, 5912–5920; (e) E. Z. Shhi, T. L. Feng, J. H. Bahk, Y. Pan, W. Zheng, Z. Li, G. J. Snyder, S. T. Pantelides and Y. Wu, *ES Energy Environ.*, 2018, **2**, 43–49; (f) W. Du, X. Wang, J. Zhan, X. Sun, L. Kang, F. Jiang, X. Zhang, Q. Shao, M. Dong, H. Liu, V. Murugadoss, Z. Guo, *Electrochim. Acta*, 2019, **296**, 907–915; (g) H. Du, C. Zhao, J. Lin, Z. Hu, Q. Shao, J. Guo, B. Wang, D. Pan, E. Wujcik and Z. Guo, *Chem. Rec.*, 2018, **18**, 1365–1372; (h) Y. Qian, Y. Yuan, H. Wang, H. Liu, J. Zhang, S. Shi, Z. Guo and N. Wang, *J. Mater. Chem. A*, 2018, **6**, 24676–24685; (i) W. Deng, T. Kang, H. Liu, J. Zhang, N. Wang, N. Lu, Y. Ma, A. Umar and Z. Guo, *Sci. Adv. Mater.*, 2018, **10**, 937–949; (j) J. Tian, Q. Shao, X. Dong, J. Zheng, D. Pan, X. Zhang, H. Cao, L. Hao, J. Liu and Z. Guo, *Electrochim. Acta*, 2018, 261, 236–245.
- 3 (a) X. H. Cao, C. L. Tan, X. Zhang, W. Zhao and H. Zhang, *Adv. Mater.*, 2016, **28**, 6167–6196; (b) J. Ren, Q. Luo, Q. Hou, H. Chen, T. Liu, H. He, J. Wang, Q. Shao, M. Dong, S. Wu, N. Wang, J. Lin, and Z. Guo, *Chemelectrochem*, 2019, in press, doi: 10.1002/celc.201900688; (c) K. Le, Z. Wang, F. Wang, Q. Wang, Q. Shao, V. Murugadoss, S. Wu, W. Liu, J. Liu, Q. Gao, and Z. Guo, *Dalton Transactions*, 2019, **48**, 5193 - 5202; (d) Y. Ma, C. Hou, H. Zhang, Q. Zhang, H. Liu, S. Wu and Z. Guo, *Electrochim. Acta*, 2019, **315**, 114–123; (e) M. Idrees, S. Batool, J. Kong, Q. Zhuang, H. Liu, Q. Shao, N. Lu, Y. Feng, E. K. Wujcik, Q. Gao, T. Ding, R. Wei, and Z. Guo, *Electrochim. Acta*, 2019, **296**, 925–937; (f) B. Kirubasankar, V. Murugadoss, J. Lin, T. Ding, M. Dong, H. Liu, J. Zhang, T. Li, N. Wang, Z. Guo and S.

- Angaiaha, *Nanoscale*, 2018, **10**, 20414 - 20425; (g) H. Wei, H. Wang, Y. Xia, D. Cui, Y. Shi, M. Dong, C. Liu, T. Ding, J. Zhang, Y. Ma, N. Wang, Z. Wang, Y. Sun, R. Wei and Z. Guo, *J. Mater. Chem. C*, 2018, **6**, 12446-12467; (h) K. Sun, R. Fan, X. Zhang, Z. Zhang, Z. Shi, N. Wang, P. Xie, Z. Wang, G. Fan, H. Liu, C. Liu, T. Li, C. Yan and Z. Guo, *J. Mater. Chem. C*, 2018, **6**, 2925-2943; (i) M. Idrees, S. Batool, Q. Zhuang, J. Kong, I. Seok, J. Zhang, H. Liu, V. Murugadoss, Q. Gao, and Z. Guo, *Ceram. Int.*, 2019, **45**, 10572-10580.
- 4 (a) J. Zhang, Z. Zhang, Y. Jiao, H. Yang, Y. Li, J. Zhang and P. Gao. *J. Power Sources*, 2019, **419**,99-105; (b) C. Hou, Z. Tai, L. Zhao, Y. Zhai, Y. Hou, Y. Fan, F. Dang, J. Wang, H. Liu, *J. Mater. Chem. A*, 2018, **6**, 9723-9736; (c) V. Murugadoss, P. Panneerselvam, C. Yan, Z. Guo and S. Angaiah, *Electrochim. Acta*, 2019, 312, 157-167; (d) C. Shen, X. Liu, H. Cao, Y. Zhou, J. Liu, J. Tang, X. Guo, H. Huang, X. Chen, *Appl. Sci.*, 2019, **9(8)**, 1708; (e) X. Lou, C. Lin, Q. Luo, J. Zhao, B. Wang, J. Li, Q. Shao, X. Guo, N. Wang and Z. Guo, *ChemElectroChem*, 2017, 4, 3171-3180; (f) Q. Hou, J. Ren, H. Chen, P. Yang, Q. Shao, M. Zhao, X. Zhao, H. He, N. Wang, Q. Luo and Z. Guo, *ChemElectroChem*, 2018, 5, 726-731; (g) C. Lin, H. Hu, C. Cheng, K. Sun, X. Guo, Q. Shao, J. Li, N. Wang and Z. Guo, *Electrochim. Acta*, 2018, **260**, 65-72; (h) L. Yang, X. Wang, X. Mai, T. Wang, C. Wang, X. Li, V. Murugadoss, Q. Shao, S. Angaiah, Z. Guo, *J. Colloid Interf. Sci.*, 2019, **534**, 459-468; (i) C. Wang, B. Mo, Z. He, Q. Shao, D. Pan, E. Wujick, J. Guo, X. Xie, X. Xie, and Z. Guo, *J. Membrane Sci.*, 2018, **556**, 118–125; (j) C. Wang, B. Mo, Z. He, C. X. Zhao, L. Zhang, Q. Shao, X. Guo, E. Wujcik, and Z. Guo, *Polymer*, 2018, **138**, 363-368; (k) Z. Qu, M. Shi, H. Wu, Y. Liu, J. Jiang, C. Yan, *J. Power Sources*, 2019, **410-411**, 179-187.
- 5 (a) M. C. Acevedo, M. L. Stone, J. R. Schmidt, J. G. Thomas, Q. Ding, H. C. Chang, M. L. Tsai, J. H. He and S. Jin, *Nature Mater.*, 2015, **14**, 1245–1251; (b) B. Lin, Z. Lin, S. Chen, M. Yu, W. Li, Q. Gao, M. Dong, Q. Shao, S. Wu, T. Ding, and Z. Guo, *Dalton Transact.*, 2019, **48**, 8279 - 8287 (c) J. Brilllet, J. H. Yum, M. Cornuz, T. Hisatomi, R. Solarska, J. Augustynsk, M. Graetzel and K. Sivula, *Nat. Photonics*, 2012, **6**, 824–828;
- 6 (a) L. Wei, K. Lozano, Y. Mao, *Eng. Sci.*, 2018, **3**, 62-66; (b) Z. Lin, B. Lin, Z. Wang, S. Chen, C. Wang, M. Dong, Q. Gao, Q. Shao, S. Wu, T. Ding, H. Liu, and Z. Guo, *Chemcatchem*, 2019, **11**, 2217– 2222; (c) C. Wang, F. Lan, Z. He, X. Xie, Y. Zhao, H. Hou, L. Guo, V. Murugadoss, H. Liu, Q. Shao, Q. Gao, *Chemsuschem*, 2019, **12**, 1576-1590; (d) J. D. desai, P. K. Baviskar, K. N. Hui and H. M. Pathan, *ES Energy Environ.*, 2018, **2**, 21-30; (e) M. Gratzel, *Nature*, 2001, **414**, 338–344; (c) T. Su, Q. Shao, Z. Qin, Z. Guo and Z. Wu, *ACS Catalysis*, 2018, **8**, 2253-2276.
- 7 A. J. Nozik, *Ann. Rev. Phys. Chem.*, 1978, **29**, 189–222
- 8 A. Fujishima and K. Honda, *Nature*, 1972, **238**, 37–38
- 9 S. C. Riha, B. M. Klahr, Eric C. Tyo, S. Seifert, S. Vajda, M. J. Pellin, T. W. Hamann and A. B. F. Martinson, *ACS Nano*, 2013, **3**, 2396–2405
- 10 J. R. Wang and F. E. Osterloh, *J. Mater. Chem. A*, 2014, **2**, 9405–9411
- 11 J. Song, J. Cha, M. G. Lee, H. W. Jeong, S. Seo, J. A. Yoo, T. L. Kim, J. Lee, H. No, D. H. Kim, S. Y. Jeong, H. An, B. H. Lee, C. W. Bark, H. Park, H. W. Jang and S. Lee, *J. Mater. Chem. A*, 2017, **5**, 18831–18838

- 12 T. W. Kim and K. S. Choi, *Science*, 2014, **343**, 990–994
- 13 G. L. Chiarello, M. Bernareggi, M. Pedroni, M. Magni, S. M. Pietralunga, A. Tagliaferri, E. Vassallo and E. Selli, *J. Mater. Chem. A*, 2017, **5**, 12977–12989
- 14 X. J. Shi, L. L. Cai, I. Y. Choi, M. Ma, K. Zhang, J. H. Zhao, J. K. Kim, J. K. Kim, X. L. Zheng and J. H. Park, *J. Mater. Chem. A*, 2018, **6**, 19542–19546
- 15 Y. Y. Bu, J. Ren, H. W. Zhang, D. J. Yang, Z. Y. Chen and J. P. Ao, *J. Mater. Chem. A*, 2018, **6**, 8604–8611
- 16 A. J. Nozik, *Nature*, 1975, **257**, 383–386
- 17 B. H. Zhou, X. F. Li, T. X. Fan, F. E. Osterloh, J. Ding, E. M. Sabio, D. Zhang and Q. X. Guo, *Adv. Mater.*, 2010, **22**, 951–956
- 18 C. M. Pelicano and H. Yanagi, *J. Mater. Chem. C*, 2017, **5**, 8059–8070
- 19 H. C. Yang, J. J. Li, L. Yu, B. B. Huang, Y. D. Ma and Y. Dai, *J. Mater. Chem. A*, 2018, **6**, 4161–4166
- 20 L. Pei, Z. Xu, S. C. Yan and Z. G. Zou, *J. Mater. Chem. A*, 2017, **5**, 12848–12855
- 21 F. A. Frame, T. K. Townsend, R. L. Chamousis, E. M. Sabio, T. Dittrich, N. D. Browning and F. E. Osterloh, *J. Am. Chem. Soc.*, 2011, **133**, 7264–7267
- 22 T. K. Townsend, N. D. Browning and F. E. Osterloh, *ACS Nano*, 2012, **6**, 7420–7426
- 23 M. Moniruddin, K. Afroz, Y. Shabdan, B. Bizri and N. Nuraje, *Appl. Surf. Sci.*, 2017, **419**, 886–892
- 24 M. Zhong, T. Hisatomi, Y. Sasaki, S. Suzuki, K. Teshima, M. Nakabayashi, N. Shibata, H. Nishiyama, M. Katayama, T. Yamada and K. Domen, *Angew. Chem. Int. Ed.*, 2017, **56**, 4739–4743
- 25 J. Song, T. L. Kim, J. Lee, S. Y. Cho, J. Cha, S. Y. Jeong, H. An, W. S. Kim, Y. S. Jung, J. Park, G. Y. Jung, D. Y. Kim, J. Y. Jo, S. D. Bu, H. W. Jang and S. H. Lee, *Nano Res.*, 2018, **11**, 642–655
- 26 F. A. Frame and F. E. Osterloh, *J. Phys. Chem. C*, 2010, **114**, 10628–10633
- 27 O. Khaselev and J. A. Turner, *Science*, 1998, **280**, 425–427
- 28 B. Song, T. T. Wang, H. G. Sun, Q. Shao, J. K. Zhao, K. K. Song, L. H. Hao, L. Wang, Z. H. Guo, *Dalton Trans.*, 2017, **46**, 15769–15777
- 29 X. Y. Feng, Y. B. Chen, Z. X. Qin, M. L. Wang and L. J. Guo, *ACS Appl. Mater. Interfaces*, 2016, **8**, 18089–18096
- 30 D. S. Martínez, A. M. D. L. Cruz and E. L. C. Illar, *Appl. Catal. A: Gen.*, 2011, **398**, 179–186
- 31 Y. Peng, Q. G. Chen, D. Wang, H. Y. Zhou and A. W. Xu, *CrystEngComm*, 2015, **17**, 569–576

- 32 S. C. Wang, H. J. Chen, G. P. Gao, T. Butburee, M. Q. Lyu, S. Thaweesak, J. H. Yun, A. Du, G. Liu and L. Z. Wang, *Nano Energy*, 2016, **24**, 94–102
- 33 G. M. Wang, Y. C. Ling, H. Y. Wang, X. Y. Yang, C. C. Wang, J. Z. Zhang and Y. Li, *Energy Environ. Sci.*, 2012, **5**, 6180–6187
- 34 F. E. Osterloh, *Chem. Soc. Rev.*, 2013, **42**, 2294–2320
- 35 X. B. Huang, G. X. Zhao and G. Wang, *J. Mater. Chem. A*, 2017, **5**, 24631–24635
- 36 P. M. Rao, I. S. Cho and X. L. Zheng, *P. Combust. Inst.*, 2013, **34**, 2187–2195
- 37 S. C. Warren, K. Voitchovsky, H. Dotan, C. M. Leroy, M. Cornuz, F. Stellacci, C. Hebert, A. Rothschild and M. Gratzel, *Nature Mater.*, 2013, **12**, 842–849
- 38 W. J. Li, P. M. Da, Y. Y. Zhang, Y. C. Wang, X. Lin, X. G. Gong and G. F. Zheng, *ACS Nano*, 2014, **8**, 11770–11777
- 39 J. Zhang, Z. H. Liu and Z. F. Liu, *ACS Appl. Mater. Interfaces*, 2016, **8**, 9684–9691
- 40 J. A. Seabold and K. S. Choi, *Chem. Mater.*, 2011, **23**, 1105–1112
- 41 Q. Y. Zeng, J. H. Li, J. Bai, X. J. Li, L. G. Xia and B. X. Zhou, *Appl. Catal. B: Environ.*, 2017, **202**, 388–396
- 42 S. C. Wang, J. H. Yun, B. Luo, T. Butburee, P. Peerakiatkhajohn, S. Thaweesak, M. Xiao and L. Z. Wang, *J. Mater. Sci. & Technol.*, 2017, **33**, 1–22
- 43 M. D. Bhatt and J. S. Lee, *J. Mater. Chem. A*, 2015, **3**, 10632–10659
- 44 T. Hisatomi, J. Kubota and Kazunari Domen, *Chem. Soc. Rev.*, 2014, **43**, 7520–7535
- 45 M. Moniruddin, B. Ilyassov, X. Zhao, E. Smith, T. Serikov, N. Ibrayev, R. Asmatulu and N. Nuraje, *Mater. Today Energy*, 2018, **7**, 246–259
- 46 K. Maeda, *ACS Catal.*, 2013, **3**, 1486–1503
- 47 Z. Chen, T. F. Jaramillo, T. G. Deutsch, A. Kleiman-Shwarsstein, A. J. Forman, N. Gaillard, R. Garland, K. Takanabe, C. Heske, M. Sunkara, E. W. McFarland, K. Domen, E. L. Miller, J. A. Turner and H. N. Dinh, *J. Mater. Res.*, 2010, **25**, 4–16
- 48 L. M. Peter and K. G. U. Wijayantha, *ChemPhysChem*, 2014, **15**, 1983–1995
- 49 M. T. Nenadovic, T. Rajh, O. I. Micic and A. J. Nozik, *J. Phys. Chem.* 1984, **88**, 5827–5830
- 50 C. A. Bignozzi, S. Caramor, V. Cristino, R. Argazzi, L. Meda and A. Tacca, *Chem. Soc. Rev.*, 2013, **42**, 2228–2246
- 51 F. L. Formal, S. R. Pendlebury, M. Cornuz, S. D. Tilley, M. Gratzel and J. R. Durrant, *J. Am. Chem. Soc.*, 2014, **136**, 2564–2574
- 52 J. Y. Gan, X. H. Lu and Y. X. Tong, *Nanoscale*, 2014, **6**, 7142–7164

- 53 K. Afroz, M. Moniruddin, N. Bakranov, S. Kudaibergenov and N. Nuraje, *J. Mater. Chem. A*, 2018, **6**, 21696–21718
- 54 E. M. Sabio, R. L. Chamousis, N. D. Browning and F. E. Osterloh, *J. Phys. Chem. C*, 2012, **116**, 3161–3170.
- 55 M. R. Waller, T. K. Townsend, J. Zhao, E. M. Sabio, R. L. Chamousis, N. D. Browning and F. E. Osterloh, *Chem. Mater.*, 2012, **24**, 698–704
- 56 J. Z. Su, X. J. Feng, J. D. Sloppy, L. J. Guo and C. A. Grimes, *Nano Lett.*, 2011, **11**, 203–208
- 57 S. S. Kalanur, Y. J. Hwang, S. Y. Chae and O. S. Joo, *J. Mater. Chem. A*, 2013, **1**, 3479–3488
- 58 H. Qi, J. Wolfe, D. P. Wang, H. J. Fan, D. Fichou and Z. Chen, *Nanoscale*, 2014, **6**, 13457–13462
- 59 M. G. Lee, D. H. Kim, W. Sohn, C. W. Moon, H. Park, S. Lee and H. W. Jang, *Nano Energy*, 2016, **28**, 250–260
- 60 S. Shin, H. S. Han, J. S. Kim, I. J. Park, M. H. Lee, K. S. Hong and I. S. Cho, *J. Mater. Chem. A*, 2015, **3**, 12920–12926
- 61 C. Santato, M. Ulmann and J. Augustynski, *Adv. Mater.*, 2001, **13**, 511–514
- 62 V. Chakrapani, J. Thangala and M. K. Sunkara, *Int. J. Hydrogen Energy*, 2009, **34**, 9050–9059
- 63 I. S. Cho, H. S. Han, M. Logar, J. Park and X. L. Zheng, *Adv. Energy Mater.*, 2016, **6**, 1501840–1501848
- 64 J. Yang, W. Z. Li, J. Li, D. B. Sun and Q. Y. Chen, *J. Mater. Chem.*, 2012, **22**, 17744–17752
- 65 F. Amano, D. Li and B. Ohtani, *Chem. Commun.*, 2010, **46**, 2769–2771
- 66 D. D. Qin, C. L. Tao, S. In, Z. Y. Yang, T. E. Mallouk, N. Z. Bao and C. A. Grimes, *Energy Fuels*, 2011, **25**, 5257–5263
- 67 J. J. Zhang, X. X. Chang, C. C. Li, A. Li, S. S. Liu, T. Wang and J. L. Gong, *J. Mater. Chem. A*, 2018, **6**, 3350–3354
- 68 S. J. Hong, H. Jun, P. H. Borse and J. S. Lee, *Int. J. Hydrogen Energy*, 2009, **34**, 3234–3242
- 69 W. Z. Li, J. Li, X. Wang, J. Ma and Q. Y. Chen, *Int. J. Hydrogen Energy*, 2010, **35**, 13137–13145
- 70 C. Fàbrega, S. Murcia-López, D. Monllor-Satoca, J.D. Prades, M.D. Hernández-Alonso, G. Penelas, J.R. Morante and T. Andreu, *Appl. Catal. B: Environ.*, 2016, **189**, 133–140
- 71 C. W. Wang, C. F. Tang, X. Y. Zhang, L. Qian and H. G. Yang, *Prog. Nat. Sci-Mater.*, 2018, **28**, 200–204
- 72 J. H. Kim, B. J. Lee, P. Wang, M. H. Son and J. S. Lee, *Appl. Catal. A: Gen.*, 2016, **521**, 233–239

- 73 M. S. Gudiksen, L. J. Lauhon, J. F. Wang, D. C. Smith and C. M. Lieber, *Nature*, 2002, **415**, 617–620
- 74 J. R. G. Navarro, A. Mayence, J. Andrade, F. Lerouge, F. Chaput, P. Oleynikov, L. Bergström, S. Parola and A. Pawlicka, *Langmuir*, 2014, **30**, 10487–10492
- 75 Q. F. Zhang and G. Z. Cao, *Nano Today*, 2011, **6**, 91–109
- 76 B. Liu and E. S. Aydil, *J. Am. Chem. Soc.*, 2009, **131**, 3985–3990
- 77 X. L. Fan, B. Gao, T. Wang, X. L. Huang, H. Gong, H. R. Xue, H. Guo, L. Song, W. Xia and J. P. He, *Appl. Catal. A: Gen.*, 2016, **528**, 52–58
- 78 B. X. Liu, J. S. Wang, J. S. Wu, H. Y. Li, Z. F. Li, M. L. Zhou and T. Y. Zuo, *J. Mater. Chem. A*, 2014, **2**, 1947–1954
- 79 K. Zhu, N. R. Neale, A. Miedaner and A. J. Frank, *Nano Lett.*, 2007, **7**, 69–74
- 80 A. Kafizas, L. Francàs, C. S. Vazquez, M. Ling, Y. M. Li, E. Glover, L. M. Cafferty, C. Blackman, J. Darr and I. Parkin, *J. Phys. Chem. C*, 2017, **121**, 5983–5993
- 81 I. S. Cho, Z. B. Chen, A. J. Forman, D. R. Kim, P. M. Rao, T. F. Jaramillo and X. L. Zheng, *Nano Lett.*, 2011, **11**, 4978–4984
- 82 M. Park, J. H. Seo, H. Song and K. M. Nam, *J. Phys. Chem. C*, 2016, **120**, 9192–9199
- 83 H. Wang, X. Quan, Y. B. Zhang and S. Chen, *Nanotechnology*, 2008, **19**, 065704
- 84 Z. Chen, M. H. Ning, G. Ma, Q. G. Meng, Y. G. Zhang, J. W. Gao, M. L. Jin, Z. H. Chen, M. Z. Yuan, X. Wang, J. M. Liu and G. F. Zhou, *Nanotechnology*, 2017, **28**, 275401
- 85 F. Q. Zhan, J. Li, W. Z. Li, Y. S. Liu, R. R. Xie, Y. H. Yang, Y. M. Li and Q. Y. Chen, *Int. J. Hydrogen. Energ.*, 2015, **40**, 6512–6520
- 86 M. Yagi, S. Maruyama, K. Sone, K. Nagai and T. Norimatsu, *J. Solid State Chem.*, 2008, **181**, 175–182
- 87 F. Amano, M. Tian, G. S. Wu, B. Ohtani and A. Chen, *ACS Appl. Mater. Interfaces*, 2011, **3**, 4047–4052
- 88 Z. H. Jiao, J. M. Wang, L. Ke, X. W. Sun and H. V. Demir, *ACS Appl. Mater. Interfaces*, 2011, **3**, 229–236
- 89 S. Sohila, M. Geerthana, S. Prabhu, T. Pratheesya, A. Mohamed Musthafa, S. Tamilselvan and R. Ramesh, *J. Mater. Sci: Mater. Electron*, 2017, **28**, 15663–15667
- 90 F. Amano, D. Li and B. Ohtani, *J. Electrochem Soc.*, 2011, **158**, K42–K46
- 91 Y. G. Li, Y. L. Li, B. S. Sa and R. Ahuja, *Catal. Sci. Technol.*, 2017, **7**, 545–559
- 92 J. J. Zhang, P. Zhang, T. Wang and J. L. Gong, *Nano Energy*, 2015, **11**, 189–195

- 93 T. W. Kim and K. S. Choi, *Science*, 2014, 343, 990–994
- 94 X. Zhao, W. J. Luo, J. Y. Feng, M. X. Li, Z. S. Li, T. Yu and Z. G. Zou, *Adv. Energy Mater.*, 2014, **4**, 1301785
- 95 D. Chandra, K. Saito, T. Yui and M. Yagi, *Angew. Chem. Int. Ed.*, 2013, **52**, 12606–12609
- 96 Z. F. Li, G. W. Zheng, J. S. Wang, H. Y. Li, J. S. Wu and Y. C. Du, *J. Nanopart. Res.*, 2016, **18**, 98
- 97 C. X. Hou, Y. Hou, Y. Fan, Y. Zhai, Y. Wang, Z. Sun, R. Fan, F. Dang and J. Wang, *J. Mater. Chem. A*, 2018, **6**, 6967–6876
- 98 K. S. Choi, *J. Phys. Chem. Lett.* 2010, **1**, 2244–2250
- 99 K. Song, F. M. Gao, W. Y. Yang, E. Wang, Z. X. Wang and H. L. Hou, *ChemElectroChem*, 2018, **5**, 322–327
- 100 S. Hilliard, G. Baldinozzi, D. Friedrich, S. Kressman, H. Strub, V. Artero and C. L. Robert, *Sustainable Energy Fuels*, 2017, **1**, 145–153
- 101 M. Y. Cai, P. X. Fan, J. Y. Long, J. P. Han, Y. Lin, H. J. Zhang and M. L. Zhong, *ACS Appl. Mater. Interfaces*, 2017, **9**, 17856–17864
- 102 C. Santato, M. Odziemkowski, M. Ulmann and J. Augustynski, *J. Am. Chem. Soc.*, 2001, **123**, 10639–10649
- 103 S. Y. Chae, C. S. Lee, H. Jung, O. S. Joo, B. K. Min, J. H. Kim and Y. J. Hwang, *ACS Appl. Mater. Interfaces*, 2017, **9**, 19780–19790
- 104 J. Z. Su, T. Zhang and L. Wang, *J. Mater. Sci.: Mater. Electron*, 2017, **28**, 4481–4491
- 105 A. K. Nayak, Y. Sohn and D. Pradhan, *Cryst. Growth Des.*, 2017, **17**, 4949–4957
- 106 H. G. Yang, C. H. Sun, S. Z. Qiao, J. Zou, G. Liu, S. C. Smith, H. M. Cheng and G. Q. Lu, *Nature*, 2008, **453**, 638–641
- 107 X. W. Wang, G. Liu, L. Z. Wang, J. Pan, G. Q. M. Lu and H. M. Cheng, *J. Mater. Chem.*, 2011, **21**, 869–873
- 108 B. H. Wu, C. Y. Guo, N. F. Zheng, Z. X. Xie and G. D. Stucky, *J. Am. Chem. Soc.* 2008, **130**, 17563–17567
- 109 D. Q. Zhang, S. L. Wang, J. Zhu, H. X. Li and Y. F. Lu, *Appl. Catal. B: Environ.*, 2012, **123-124**, 398–404
- 110 P. Y. Dong, G. H. Hou, X. G. Xi, R. Shao and F. Dong, *Environ. Sci.: Nano*, 2017, **4**, 539–557
- 111 J. Y. Zheng, G. Song, J. S. Hong, T. K. Van, A. U. Pawar, D. Y. Kim, C. W. Kim, Z. Haider and Y. S. Kang, *Cryst. Growth Des.*, 2014, **14**, 6057–6066

- 112 R. Liu, Y. J. Lin, L. Y. Chou, S. W. Sheehan, W. S. He, F. Zhang, H. J. M. Hou and D. W. Wang, *Angew. Chem.*, 2011, **123**, 519–522
- 113 (a) W. Smith, A. Wolcott, R. C. Fitzmorris, J. Z. Zhang and Y. P. Zhao, *J. Mater. Chem.*, 2011, **21**, 10792–10800; (b) H. Sun, Z. Yang, Y. Pu, W. Dou, C. Wang, W. Wang, X. Hao, S. Chen, Q. Shao, M. Dong, S. Wu, T. Ding and Z. Guo, *J. Colloid Interf. Sci.*, 2019, **547**, 40–49; (c) Y. Sheng, J. Yang, F. Wang, L. Liu, H. Liu, C. Yan, and Z. Guo, *Appl. Surface Sci.*, 2019, 465, 154–163; (d) Z. Zhao, H. An, J. Lin, M. Feng, V. Murugadoss, T. Ding, H. Liu, Q. Shao, X. Man, N. Wang, H. Gu, S. Angaiah, and Z. Guo, *Chem. Rec.*, 2019, 19, 873–882; (e) J. Tian, Q. Shao, J. Zhao, D. Pan, M. Dong, C. Jia, T. Ding, T. Wu and Z. Guo, *J. Colloid Interf. Sci.*, 2019, **541**, 18–29; (f) L. Zhang, W. Yu, C. Han, J. Guo, Q. Zhang, H. Xie, Q. Shao, Z. Sun and Z. Guo, *J. Electrochem. Soc.*, 2017, **164**, H651–H656; (g) L. Zhang, M. Qin, W. Yu, Q. Zhang, H. Xie, Z. Sun, Q. Shao, X. Guo, L. Hao, Y. Zheng and Z. Guo, *J. Electrochem. Soc.*, 2017, **164**, H1086–H1090
- 114 (a) J. Johnson, N. Bakranov, M. Moniruddin, R. Iskakov, S. Kudaibergenov and N. Nuraje, *New J. Chem.*, 2017, **41**, 15528–15532; (b) B. Song, T. Wang, H. Sun, Q. Shao, J. Zhao, K. Song, L. Hao, L. Wang, and Z. Guo, *Dalton Trans.*, 2017, **46**, 15769–15777.
- 115 Z. F. Hu, M. K. Xu, Z. R. Shen and J. C. Yu, *J. Mater. Chem. A*, 2015, **3**, 14046–14053
- 116 Y. Ma, Y. L. Jia, L. Wang, M. Yang, Y. P. Bi and Y. X. Qia, *Appl. Surf. Sci.*, 2016, **390**, 399–405
- 117 Y. G. Li, J. Feng, H. J. Li, X. L. Wei, R. R. Wang and A. N. Zhou, *Int. J. Hydrogen. Energ.*, 2016, **41**, 4096–4105
- 118 K. H. Ng, L. J. Minggua, W. F. Mark-Lee, K. Arifin, M. H. H. Jumali and M. B. Kassim, *Mater. Res. Bulletin*, 2018, **98**, 47–52
- 119 D. P. Wang, P. S. Bassi, H. Qi, X. Zhao, Gurudayal, L. H. Wong, R. Xu, T. Sritharan and Z. Chen, *Materials*, 2016, **9**, 348
- 120 J. Zhu, W. Z. Li, J. Li, Y. M. Li, H. S. Hua, Y. H. Yang, *Electrochimica Acta*, 2013, **112**, 191–198
- 121 C. J. Liu, Y. H. Yang, W. Z. Li, J. Li, Y. M/ Li and Q. Y. Chen, *Sci. Rep.*, 2016, **6**, 23451
- 122 A. A.M. Ibrahim, I. Khan, N. Iqbal and A. Qurashi, *Int. J. Hydrogen. Energ.*, 2017, **42**, 3423–3430
- 123 Y. G. Zhou, L. Y. Zhang, L. H. Lin, B. R. Wygant, Y. Liu, Y. Zhu, Y. B. Zheng, C. B. Mullins, Y. Zhao, X. H. Zhang and G. H. Yu, *Nano Lett.*, 2017, **17**, 8012–8017
- 124 P. M. Rao, L. L. Cai, C. Liu, I. S. Cho, C. H. Lee, J. M. Weisse, P. D. Yang and X. L. Zheng, *Nano Lett.*, 2014, **14**, 1099–1105
- 125 S. Y. Chae, H. J. Jung, H. S. Jeon, B. K. Min, Y. J. Hwang and O. S. Joo, *J. Mater. Chem. A*, 2014, **2**, 11408–11416

- 126 C. W. Lai and S. Sreekantan, *Int. J. Hydrogen. Energ.*, 2013, **38**, 2156–2166
- 127 K. C. Leonard, K. M. Nam, H. C. Lee, S. H. Kang, H. S. Park and A. J. Bard, *J. Phys. Chem. C*, 2013, **117**, 15901–15910
- 128 P. D. Wu, Z. F. Liu, D. Chen, M. Zhou and J. D. Wei, *Appl. Surf. Sci.*, 2018, **440**, 1101–1106
- 129 H. S. Lin and L. Y. Lin, *Electrochimica Acta*, 2017, **252**, 235–244
- 130 J. Zhang, H. P. Ma and Z. F. Liu, *Appl. Catal. B: Environ.*, 2017, **201**, 84–91
- 131 Y. D. Wang, W. Tian, L. Chen, F. R. Cao, J. Guo and L. Li, *ACS Appl. Mater. Interfaces*, 2017, **46**, 40235–40243
- 132 C. J. Liu, Y. H. Yang, J. Li, S. Chen, W. Z. Li and X. D. Tang, *Chem. Eng. J.*, 2017, **326**, 603–611
- 133 W. L. Kwong, C. C. Lee and J. Messinger, *J. Phys. Chem. C*, 2016, **120**, 10941–10950
- 134 S. S. Kalanur, I. H. Yoo, J. Park and H. Seo, *J. Mater. Chem. A*, 2017, **5**, 1455–1461
- 135 J. Z. Su, L. J. Guo, N. Z. Bao and C. A. Grimes, *Nano Lett.*, 2011, **11**, 1928–1933
- 136 J. W. Huang, Y. Ding, X. Luo and Y. Y. Feng, *J. Catal.*, 2016, **333**, 200–206
- 137 X. P. Qi, G. W. She, Y. Y. Liu, L. X. Mua and W. S. Shi, *Chem. Commun.*, 2012, **48**, 242–244
- 138 C. J. Liu, Y. M. Li, W. Z. Li, J. Zhu, J. Li, Q. Y. Chen and Y. H. Yang, *Mater. Lett.*, 2014, **120**, 170–173
- 139 Y. W. Choi, S. Kim, M. Seong, H. Yoo and J. Choi, *Appl. Surf. Sci.*, 2015, **324**, 414–418
- 140 S. C. Wang, P. Chen, Y. Bai, J. H. Yun, G. Liu and Lianzhou Wang, *Adv. Mater.* 2018, **20**, 1800486
- 141 S. C. Wang, P. Chen, J. H. Yun, Y. X. Hu and L. Z. Wang, *Angew. Chem. Int. Ed.*, 2017, **56**, 8500–8504
- 142 B. J. Jin, E. Jung, M. Ma, S. Kim, K. Zhang, J. I Kim, Y. Son and J. H. Park, *J. Mater. Chem. A*, 2018, **6**, 2585–2592
- 143 M. G. Mali1, H. Yoon, M. Kim, M. T. Swihart, S. S. Al-Deyab and S. S. Yoon, *Appl. Phys. Lett.*, 2015, **106**, 151603.
- 144 J. H. Baek, B. J. Kim, G. S. Han, S. W. Hwang, D. R. Kim, I. S. Cho and H. S. Jung, *ACS Appl. Mater. Interfaces*, 2017, **9**, 1479–1486.
- 145 K. Zhang, X. J. Shi, J. K. Kima and J. H. Park, *Phys. Chem. Chem. Phys.*, 2012, **14**, 11119–11124

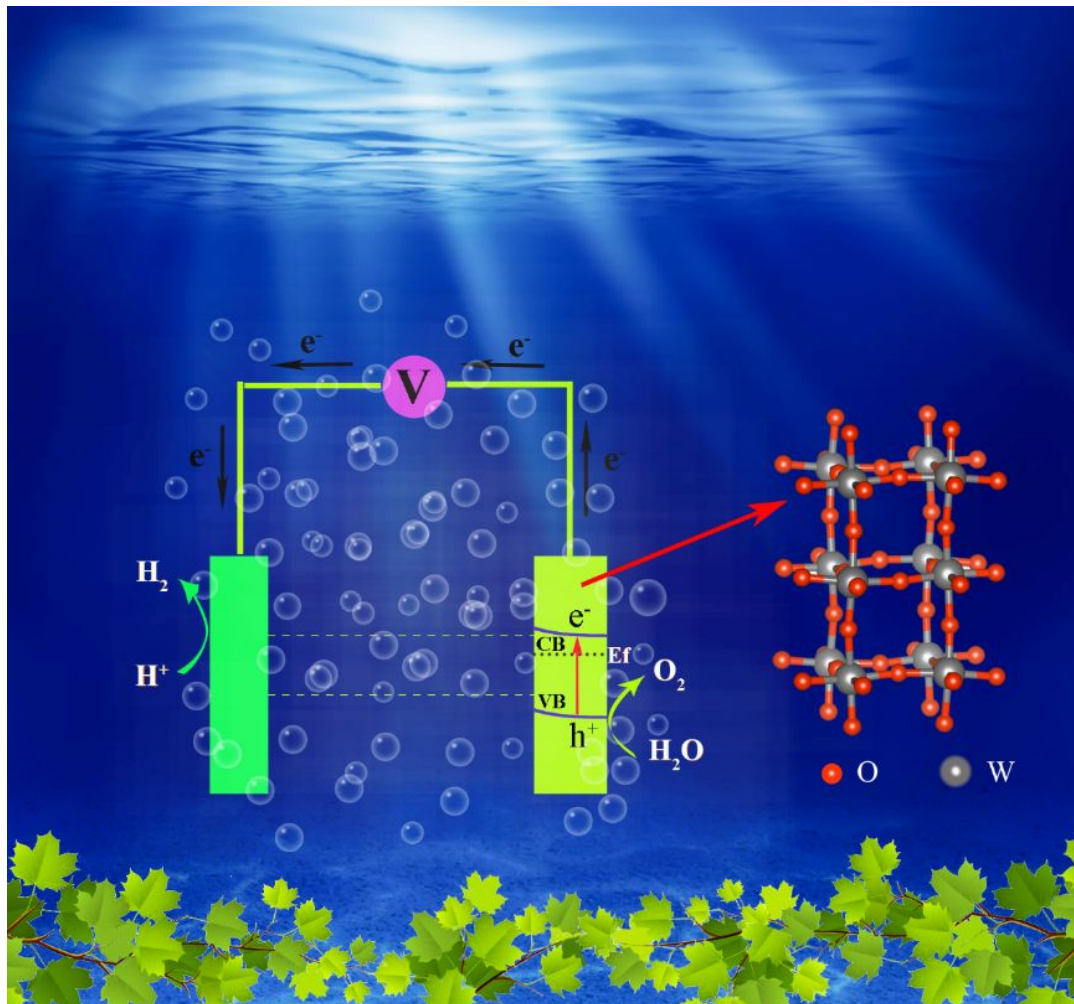
- 146 Q. Y. Zeng, J. H. Li, L. S. Li, J. Bai, L. G. Xia and B. X. Zhou, *Appl. Catal. B: Environ.*, 2017, **217**, 21–29
- 147 P. Chatchai, Y. Murakami, S.Y. Kishioka, A.Y. Nosaka and Y. Nosaka, *Electrochim. Acta*, 2009, **54**, 1147–1152
- 148 R. Saito, Y. Miseki and K. Sayama, *Chem. Commun.*, 2012, **48**, 3833–3835
- 149 J. H. Seo, G. Park, K. H. Oh, S. H. Kang, H. C. Lee, S. K. Cho and K. M. Nam, *J. Electroanal. Chem.*, 2017, **789**, 17–23
- 150 H. F. Zhang, W. W. Zhou, Y. P. Yang and C. W. Cheng, *small* 2017, **13**, 1603840
- 151 N. Iqbal, I. Khan, Z. H. A. Yamani and A. Qurashi, *Solar Energy*, 2017, **144**, 604–611
- 152 S. J. A. Moniz, S. A. Shevlin, D. J. Martin, Z. X. Guo and J. W. Tang, *Energy Environ. Sci.*, 2015, **8**, 731–759
- 153 J. H. Yang, D. G. Wang, H. X. Han and C. Li, *Acc. Chem. Res.*, 2013, **46**, 1900–1909
- 154 J. R. Ran, J. Zhang, J. G. Yu, M. Jaroniec and S. Z. Qiao, *Chem. Soc. Rev.*, 2014, **43**, 7787–7812
- 155 G. C. Xi, J. H. Ye, Q. Ma, N. Su, H. Bai and C. Wang, *J. Am. Chem. Soc.*, 2012, **134**, 6508–6511
- 156 Z. F. Liu, J. Y. Wu and J. Zhang, *Int. J. Hydrogen. Energ.*, 2016, **41**, 20529–20535
- 157 D. Y. Hu, P. Diao, D. Xu and Q. Y. Wu, *Nano Res.*, 2016, **6**, 1735–1751
- 158 F. Xu, Y. W. Yao, D. D. Bai, R. S. Xu, J. J. Mei, D. P. Wu, Z. Y. Gao and K. Jiang, *J. Colloid Interf. Sci.*, 2015, 458, 194–199
- 159 (a) Y. D. Hou, A. B. Laursen, J. S. Zhang, G. G. Zhang, Y. S. Zhu, X. C. Wang, S. Dahl and I. Chorkendorff, *Angew. Chem., Int. Ed.*, 2013, **52**, 3621–3615; (b) X. Wu, W. Li, P. Wu, C. Ma, Y. Liu, M. Xu and S. Liu, *Eng. Sci.*, 2018, **4**, 111–118.
- 160 J. Zhang, J. G. Yu, Y. M. Zhang, Q. Li and J. R. Gong, *Nano Lett.*, 2011, **11**, 4774–4779
- 161 F. A. Frame and F. E. Osterloh, *J. Phys. Chem. C*, 2010, **114**, 10628–10633
- 162 L. Zhang, Q. H. Zhang, H. Y. Xie, J. Guo, H. L. Ly, Y. G. Li, Z. G. Sun, H. Z. Wang and Z. H. Guo, *Appl. Catal. B: Environ.*, 2017, **201**, 470–478
- 163 H. Y. Zhang, W. J. Tian, Y. G. Li, H. Q. Sun, M. O. Tadé and S. B. Wang, *J. Mater. Chem. A*, 2018, **6**, 6265–6272
- 164 J. Sato, N. Saito, Y. Yamada, K. Maeda, T. Takata, J. N. Kondo, M. Hara, H. Kobayashi, K. Domen and Y. Inoue, *J. Am. Chem. Soc.*, 2005, **127**, 4150–4151
- 165 B. J. Ma, J. H. Yang, H. X. Han, J. T. Wang, X. H. Zhang and C. Li, *J. Phys. Chem. C*, 2010, **114**, 12818–12822

- 166 R. L. Lee, P. D. Tran, S. S. Pramana, S. Y. Chiam, Y. Ren, S. Y. Meng, L. H. Wong and J. Barber, *Catal. Sci. Technol.*, 2013, **3**, 1694–1698
- 167 Y. b. Wang, Y. S. Wang, R. R. Jiang and R. Xu, *Ind. Eng. Chem. Res.*, 2012, **51**, 9945–9951
- 168 J. S. Zhang, M. Grzelczak, Y. D. Hou, K. Maeda, K. Domen, X. Z. Fu, M. Antonietti and X. C. Wang, *Chem. Sci.*, 2012, **3**, 443–446
- 169 F. X. Zhang, A. Yamakata, K. Maeda, Y. Moriya, T. Takata, J. Kubota, K. Teshima, S. Oishi and K. Domen, *J. Am. Chem. Soc.*, 2012, **134**, 8348–8351
- 170 L. C. Liu, Z. Y. Ji, W. X. Zou, X. R. Gu, Y. Deng, F. Gao, C. J. Tang and L. Dong, *ACS Catal.*, 2013, **3**, 2052–2061
- 171 M. W. Kanan and D. G. Nocera, *Science*, 2008, **321**, 1072–1075
- 172 Q. Liu, Q. P. Chen, J. Bai, J. Y. Li, J. H. Li and B. X. Zhou, *J. Solid State Electrochem.*, 2014, **18**, 157–161
- 173 M. Ma, K. Zhang, P. Li, M. S. Jung, M. J. Jeong and J. H. Parkm, *Angew. Chem. Int. Ed.*, 2016, **55**, 11819–11823
- 174 L. Pei, Z. Xu, Z. Shi, H. Zhu, S. C. Yan and Z. G. Zou, *J. Mater. Chem. A*, 2017, **5**, 20439–20447
- 175 Y. Liu, Y. H. Yang, Q. Liu, H. Z. He, W. H. Liu, D. D. Meng, Y. M. Li, W. Z. Li and J. Li, *Int. J. Hydrogen. Energ.*, 2018, **43**, 208–218
- 176 Y. Liu, J. Li, H. Tang, W. Z. Li, Y. H. Yang, Y. M. Li and Q. Y. Chen, *Electrochem. Commun.*, 2016, **68**, 81–85
- 177 G. M. Wang, Y. C. Ling and Y. Li, *Nanoscale*, 2012, **4**, 6682–6691
- 178 Y. Liu, J. Li, W. Z. Li, H. Z. He, Y. H. Yang, Y. M. Li and Q. Y. Chen, *Electrochimica Acta*, 2016, **210**, 251–260
- 179 B. Cole, B. Marsen, E. Miller, Y. Yan, B. To, K. Jones and M. A. Jassim, *J. Phys. Chem. C*, 2008, **112**, 5213–5220
- 180 F. Wang, C. D. Valentin and G. Pacchioni, *J. Phys. Chem. C*, 2012, **116**, 8901–8909
- 181 S. L. Liew, Z. Zhang, T. W. G. Goh, G. S. Subramanian, H. L. D. Seng, T. S. A. Hor, H. K. Luo and D. Z. Chi, *Int. J. Hydrogen. Energ.*, 2014, **39**, 4291–4298
- 182 C. Feng, S. Wang and B. Geng, *Nanoscale*, 2011, **3**, 3695
- 183 S. S. Kalanur, I. H. Yoo, K. Y. Eom and H. Seo, *J. Catal.*, 2018, **357**, 127–137
- 184 W. Z. Li, F. Q. Zhan, J. Li, C. J. Liu, Y. H. Yang, Y. M. Li and Q. Y. Chen, *Electrochimica Acta*, 2015, **160**, 57–63
- 185 Y. H. Xia, C. Q. Xu, W. D. Zhang, *J. Solid State Electrochem.*, 2017, **21**, 3355–3364

- 186 V. Hariharan, V. Aroulmoji, K. Prabakaran, B. Gnanavel, M. Parthibavarman, R. Sathyapriya and M. Kanagaraj, *J. Alloy. Compd.*, 2016, **689**, 41–47
- 187 S. S. Kalanur and H. Seo, *J. Colloid Interf. Sci.*, 2018, **509**, 440–447
- 188 S. Sakthivel and H. Kisch, *Angew. Chem. Int. Ed.*, 2003, **42**, 4908–4911
- 189 D. Paluselli, B. Marsen, E. L. Miller and R. E. Rocheleau, *Electrochem. Solid St. Lett.*, 2005, **8**, G301–G303
- 190 W. Z. Li, J. Li, X. Wang and Q. Y. Chen, *Appl. Surf. Sci.*, 2012, **263**, 157–162
- 191 X. D. Ma, W. X. Ma, D. L. Jiang, D. Li, S. Meng and M. Chen, *J. Colloid Interf. Sci.*, 2017, **506**, 93–101
- 192 H. L. Guo, H. Du, Y. F. Jiang, N. Jiang, C. C. Shen, X. Zhou, Y. N. Liu and A. W. Xu, *J. Phys. Chem. C*, 2017, **121**, 107–114
- 193 A. Meng, B. Zhu, B. Zhong, L. Y. Zhang and B. Cheng, *Appl. Surf. Sci.*, 2017, **422**, 518–527
- 194 Z. Y. Liang, J. X. Wei, X. Wang, Y. Yu and F. X. Xiao, *J. Mater. Chem. A*, 2017, **5**, 15601–15612
- 195 A. B. Yousaf, M. Imran, S. J. Zaidi and P. Kasak, *Sci. Rep.*, 2017, **7**, 6574
- 196 P. J. Yang, J. H. Zhao, J. Wang, B. Y. Cao, L. Li and Z. P. Zhu, *J. Mater. Chem. A*, 2015, **3**, 8256–8259
- 197 Y. J. Yuan, D. Q. Chen, S. H. Yang, L. X. Yang, J. J. Wang, D. P. Cao, W. G. Tu, Z.T. Yu and Z. G. Zou, *J. Mater. Chem. A*, 2017, **5**, 21205–21213
- 198 W. J. Yin, L. J. Bai, Y. Z. Zhu, S. X. Zhong, L. H. Zhao, Z. Q. Li and S. Bai, *ACS Appl. Mater. Interf.*, 2016, **8**, 23133–23142
- 199 Y. G. Miseki, S. Fujiyoshi, T. Gunji and K. Sayama, *J. Phys. Chem. C*, 2017, **121**, 9691–9697
- 200 H. J. Li, W. G. Tu, Y. Zhou and Z. G. Zou, *Adv.Sci.*, 2016, **3**, 1500389
- 201 P. Zhou, J. G. Yu and M. Jaroniec, *Adv. Mater.*, 2014, **26**, 4920–4935
- 202 X. Y. Li, H. H. Hu, L. B. Xu, C. Cui, D. G. Qian, S. Li, W. Z. Zhu, P. Wang, P. Lin, J. Q. Pan and C. R. Li, *Appl. Surf. Sci.*, 2018, **441**, 61–68
- 203 R. Ye, H. Fang, Y. Zheng, N. Li, Y. Wang and X. Tao, *ACS Appl. Mater. Interfaces*, 2016, **8**, 13879–13889
- 204 L. J. Zhang, S. Li, B. K. Liu, D. J. Wang and T. F. Xie, *ACS Catal.*, 2014, **4**, 3724–3729
- 205 T. P. Hu, P. F. Li, J. F. Zhang, C. H. Liang and K. Dai, *Appl. Surf. Sci.*, 2018, **442**, 20–29
- 206 J. Ding, W. Xu, H. Wan, D. S. Yuan, C. Chen, L. Wang, G. F. Guan and W. L. Dai, *Appl. Catal. B: Environ.*, 2018, **221**, 626–634

- 207 X. Lu, Z. F. Liu, J. W. Li, J. Zhang and Z. G. Guo, *Appl. Catal. B: Environ.*, 2017, **209**, 657–662
- 208 P. Wu, J. R. Wang, J. Zhao, L. J. Guo and F. E. Osterloh, *J. Mater. Chem. A*, 2014, **2**, 20338–20344.
- 209 G. X. Zhao, X. B. Huang, F. Fina, G. Zhang and J. T. S. Irvine, *Catal. Sci. Technol.*, 2015, **5**, 3416–3422
- 210 X. Li, J. G. Yu, J. X. Low, Y. P. Fang, J. Xiao and X. B. Chen, *J. Mater. Chem. A*, 2015, **3**, 2485–2534
- 211 H. J. Yan, X. J. Zhang, S. Q. Zhou, X. H. Xie, Y. L. Luo and Y. H. Yu, *J. Alloy. Compd.*, 2011, **509**, L232–L235
- 212 Z. Y. Jin, N. Murakami, T. Tsubota and T. Ohno, *Appl. Catal. B: Environ.*, 2014, **150–151**, 479–485
- 213 H. Katsumata, Y. Tachi, T. Suzuki and S. Kaneco, *RSC Adv.*, 2014, **4**, 21405
- 214 W. Y. Zhu, F. Q. Sun, R. Goei and Y. Zhou, *Catal. Sci. Technol.*, 2017, **7**, 2591
- 215 T. T. Xiao, Z. Tang, Y. Yang, L. Q. Tang, Y. Zhou and Z. G. Zou, *Appl. Catal. B: Environ.*, 2018, **220**, 417–428
- 216 L. F. Cui, X. Ding, Y. G. Wang, H. C. Shi, L. H. Huang, Y. H. Zuo and S. F. Kang, *Appl. Surf. Sci.*, 2017, **391**, 202–210
- 217 C. H. Wang, D. D. Qin, D. L. Shan, J. Gu, Y. Yan, J. Chen, Q. H. Wang, C. H. He, Y. Li, J. J. Quan and X. Q. Lu, *Phys. Chem. Chem. Phys.*, 2017, **19**, 4507–4515
- 218 W. L. Yu, J. X. Chen, T. T. Shang, L. F. Chen, L. Gu and T. Y. Peng, *Appl. Catal. B: Environ.*, 2017, **219**, 693–704

Table of Contents Entry



This paper reviews nanostructural tungsten oxides and their nanocomposites to enhance the activity of photoelectrochemical water splitting